J. Fluid Mech. (2001), *vol.* 426, *pp.* 263–295. Printed in the United Kingdom

Flow past a square-section cylinder with a wavy stagnation face

By RUPAD M. DAREKAR AND SPENCER J. SHERWIN

Department of Aeronautics, Imperial College of Science, Technology and Medicine, London, SW7 2BY, UK

(Received 6 March 2000 and in revised form 4 August 2000)

Numerical investigations have been performed for the flow past square-section cylinders with a spanwise geometric deformation leading to a stagnation face with a sinusoidal waviness. The computations were performed using a spectral/*hp* element solver over a range of Reynolds numbers from 10 to 150.

Starting from fully developed shedding past a straight cylinder at a Reynolds number of 100, a sufficiently high waviness is impulsively introduced resulting in the stabilization of the near wake to a time-independent state. It is shown that the spanwise waviness sets up a cross-flow within the growing boundary layer on the leading-edge surface thereby generating streamwise and vertical components of vorticity. These additional components of vorticity appear in regions close to the inflection points of the wavy stagnation face where the spanwise vorticity is weakened. This redistribution of vorticity leads to the breakdown of the unsteady and staggered Kármán vortex wake into a steady and symmetric near-wake structure. The steady nature of the near wake is associated with a reduction in total drag of about 16% at a Reynolds number of 100 compared with the straight, non-wavy cylinder.

Further increases in the amplitude of the waviness lead to the emergence of hairpin vortices from the near-wake region. This wake topology has similarities to the wake of a sphere at low Reynolds numbers. The physical structure of the wake due to the variation of the amplitude of the waviness is identified with five distinct regimes. Furthermore, the introduction of a waviness at a wavelength close to the mode A wavelength and the primary wavelength of the straight square-section cylinder leads to the suppression of the Kármán street at a minimal waviness amplitude.

1. Introduction

Bluff bodies are found in many engineering applications, including heat exchangers, risers in marine technology, road vehicles, buildings and bridges. Their wakes can generate large unsteady forces which have the potential to violently damage the structural integrity of the bluff body. For this reason, many methods have been proposed over the recent years to control the wake vortex dynamics with the aim of weakening the vortex shedding and reducing the amplitude of the fluctuating lift as well as the drag.

Nominally two-dimensional methods such as splitter plates (Roshko 1955; Bearman 1965) and base bleed (Bearman 1967) have been successfully used in the past to suppress vortex shedding and reduce the base drag. These studies suggest that the effect of the splitter plate and base bleed is to delay the upper and lower separated shear layers interacting with each other and hence they increase the formation length (position at which the vortices are fully formed or, in a time-average sense, the length

of the mean recirculation region). As discovered by Bearman (1965), the base pressure varies linearly with the inverse of the formation length. Hence, the increase in the formation length results in a reduction of the suction near the base of the cylinder and hence reduces the base drag.

Three-dimensional methods that achieve similar effects have also been proposed. Naumann, Morsbach & Kramer (1966) showed that vortex shedding could be suppressed by using broken and corrugated separation wires as well as a forced step in the separation line along the span of a circular cylinder at a supercritical Reynolds number of 500 000. Tanner (1972) continued the work of Naumann *et al.* (1966) by introducing a broken separation line along the trailing edge of a blunt aerofoil. He applied a stepwise deformation to the trailing edge and observed that by increasing the depth of the steps, larger base drag reductions are obtained. The maximum drag reduction obtained using this method was 64%. However, no explanation of the aerodynamic mechanisms which are responsible for the drag reduction was given. The study of this drag reduction technique (segmented trailing edge) was then continued by Rodriguez (1991) and Petrusma & Gai (1994, 1996).

Bearman & Tombazis (1993) and Tombazis & Bearman (1997) investigated the three-dimensional features of the wake behind a blunt-based model with a wavy trailing edge at a Reynolds number of 40 000. For a two-dimensional body at high Reynolds numbers, it was noted that vortex dislocations appeared in the wake apparently randomly in time and spanwise position. However, they observed that the introduction of a spanwise waviness at the trailing edge fixed the positions of these vortex dislocations along the span of the body. They found that by increasing the wave steepness, defined as the ratio of peak-to-peak wave height divided by the wavelength, the base pressure was increased which resulted in a drag reduction. The maximum drag reduction of 34% at a Reynolds number of 40 000 occurred for a wave steepness of 0.14 (the non-dimensional wavelength, defined as the wavelength divided by the base height, was equal to 3.5). Based on these facts, they concluded that encouraging the formation of dislocations in the wake reduces the drag.

More recently Bearman & Owen (1998*a*, *b*) continued the above work but this time applied the waviness at the leading edge only for rectangular cross-section bodies. Wavy flat plates were also investigated. They observed that a mild disturbance (wave steepness of only 0.06 to 0.09) resulted in the complete suppression of vortex shedding and substantial drag reduction of at least 30% at a Reynolds number of 40 000 (the non-dimensional wavelength was equal to 5.6). Also, a large variation in the wake width across the span was reported. The reasons for these observations are not yet understood and are the subject of the present work.

The aim of the current work is to carry out well-resolved numerical simulations of the flow past three-dimensional bluff bodies with a sinusoidal stagnation surface. The geometries used in this work have both front and rear faces sinusoidal. However, in the work of Bearman & Owen (1998*a*, *b*), only the front face was wavy for the rectangular cross-section bodies. In their experiments, similar results were also obtained with a flat plate which has both front and rear faces wavy. This latter result would suggest that the wavy trailing edge does not influence the qualitative observations made during the experiments of Bearman & Owen (1998*a*, *b*). It is found that accurate computations obtained directly from the Navier–Stokes equations greatly contribute to an understanding of the fundamental issues regarding the vortex dynamics occurring in the wake of such complex three-dimensional bodies. Most of the simulations in this paper have been done at a Reynolds number of 100 although for purposes of comparison additional Reynolds numbers of 10, 30 and 150 were used.

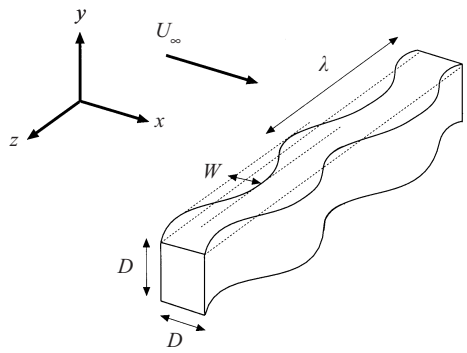

FIGURE 1. Schematic of the cylinder with the waviness at both the leading and trailing edge surfaces.

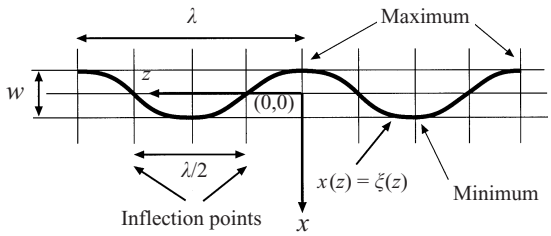

FIGURE 2. Specification of the waviness of the centreline (plan view).

This paper is outlined as follows. Section 2 details the problem definition and introduces the non-dimensional parameters. In § 3, we introduce the mapping employed to handle the waviness. We include more details about the numerical method as well as a resolution study for the flow investigations in the Appendix. In § 4, we present the main results of the effect of varying the amplitude of the waviness in terms of the forces and flow regimes. A physical interpretation of the non-dimensional parameters describing the waviness is introduced and the effect of the initial conditions is also investigated. In this study, the method proposed by Jeong & Hussain (1995) to identify vortical regions is used to elucidate the wake topology. Finally, we present a discussion in § 5 and conclude in § 6.

2. Parametric definition of the geometric body

We are interested in the flow past a square-section cylinder with a waviness in both the front and rear faces as shown in figure 1. The wavy cylinder is defined by the peak-to-peak wave height W, the wavelength λ and the base height D. The free-stream velocity U_∞ is aligned with the x-axis (streamwise direction), the span of the cylinder is aligned with the z-axis (spanwise or cross-flow direction) and finally the y-axis will be denoted as the vertical direction. We define the Reynolds number based on the base height D, as $Re = U_\infty D/\nu$ where ν is the kinematic viscosity of the fluid. A plan view of the waviness of the centreline (defined as a line through the centroid of the body along the span) is shown in figure 2. The maximum denotes the most upstream cross-section (peak), while the minimum denotes the most downstream cross-section (valley). Furthermore, with reference to figure 2, the waviness of the centreline can be

expressed mathematically in the following form:

$$\xi(z) = -\frac{W}{2}\cos\left(\frac{2\pi}{\lambda}z\right). \tag{2.1}$$

2.1. *Dimensionless length scales*

In contrast to the standard flow past a non-wavy cylinder, we have now introduced two extra length scales W and λ. Whilst the non-wavy case can be completely characterized by the Reynolds number based upon the base height D, we now have a further two independent length parameters that we choose to define as W/λ and λ/D. Further, differentiating equation (2.1) with respect to z gives an expression for the slope of the waviness $\mathrm{d}\xi/\mathrm{d}z$:

$$\frac{\mathrm{d}\xi}{\mathrm{d}z} = \pi\frac{W}{\lambda}\sin\left(\frac{2\pi}{\lambda}z\right) = A_s\sin\left(\frac{2\pi}{\lambda}z\right) \tag{2.2}$$

where $A_s = \pi W/\lambda$ is the maximum magnitude of the slope and depends on W/λ which is defined as the wave steepness by Bearman & Owen (1998*a*, *b*). The slope of the waviness, which is proportional to the wave steepness, reaches a maximum value of A_s at the inflection points $z = \frac{1}{4}\lambda, \frac{3}{4}\lambda$ shown in figure 2.

3. Computational method

A parallel spectral element code $\mathcal{N}\boldsymbol{\varepsilon\kappa}\mathcal{T}\boldsymbol{\alpha r}$ (Sherwin & Karniadakis 1995; Warburton 1998; Karniadakis & Sherwin 1999) was employed to solve the three-dimensional incompressible Navier–Stokes equations. Spectral element methods have been widely used in the past for the prediction of bluff body flows (Karniadakis & Triantafyllou 1992; Henderson & Karniadakis 1995; Henderson & Barkley 1996; Thompson, Hourigan & Sheridan 1996; Henderson 1997) due to their high temporal and spatial accuracy. Solution refinement can be obtained either by refining the mesh (h-refinement) or increasing the polynomial order P (P-refinement). A brief overview of the algorithm as well as a convergence study is presented in the Appendix. Before proceeding to the results section, we will discuss the use of a geometric mapping employed in the current work.

3.1. *Mapping from a wavy to a straight cylinder*

An efficient approach to the computation of the flow past three-dimensional bodies (as far as CPU time is concerned) is possible when the cross-section of the body is constant along the span, such as the geometry shown in figure 1. In this approach, a spectral element discretization is used only in the (x, y)-plane while a Fourier expansion is used in the spanwise z-direction. Hence, periodic boundary conditions have to be specified in the spanwise direction. This method is often referred to as the spectral element/Fourier method. Only a two-dimensional mesh is required which is a considerable advantage when compared to a full three-dimensional approach.

The waviness is introduced via a mapping previously adopted by Newman (1996) and Evangelinos (1999). The mapping transforms the deformed body into a non-deformed body as shown in figure 3. Therefore, in the transformed coordinate system (x, y, z) the geometry appears straight. In an inertial reference frame (x', y', z'), the non-dimensional Navier–Stokes equations can be written as

$$\frac{\partial \boldsymbol{u}'}{\partial t} + (\boldsymbol{u}'\cdot\nabla')\boldsymbol{u}' = -\nabla' p' + \frac{1}{Re}\nabla'^2\boldsymbol{u}', \tag{3.1}$$

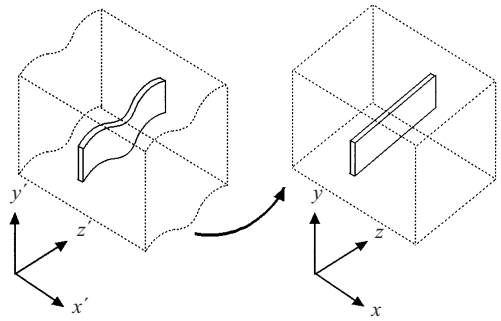

FIGURE 3. Transformation of the computational domain from an inertial system x', y', z' where the domain boundaries are deformed to the non-deformed domain x, y, z.

$$\nabla' \cdot \boldsymbol{u}' = 0, \tag{3.2}$$

where $\boldsymbol{u}' = u'\boldsymbol{i}' + v'\boldsymbol{j}' + w'\boldsymbol{k}'$ is the velocity vector, p' is the static pressure, Re is the Reynolds number and ∇' is the gradient operator in the inertial reference frame. Lengths are scaled by the cylinder base height D and the velocities by the free-stream velocity U_∞. The transformation is then defined as:

$$x = x' - \xi(z'), \quad y = y', \quad z = z', \tag{3.3}$$

where $\xi(z')$ is the streamwise displacement of the cylinder given by $\xi(z) = -\frac{1}{2}W\cos((2\pi/\lambda)z)$. By differentiating (3.3) and applying the chain rule, the velocities and pressure are then transformed as: $u = u' - w'\partial\xi/\partial z$, $v = v'$, $w = w'$ and $p = p'$. The Navier–Stokes and continuity equations in terms of the transformed coordinates and velocities then become (see Newman 1996 for more details)

$$\left.\begin{aligned} \frac{\partial \boldsymbol{u}}{\partial t} + (\boldsymbol{u}\cdot\nabla)\boldsymbol{u} &= -\nabla p + \frac{1}{Re}\nabla^2\boldsymbol{u} + \boldsymbol{A}(\boldsymbol{u}, p, \xi), \\ \nabla\cdot\boldsymbol{u} &= 0, \end{aligned}\right\} \tag{3.4}$$

where $\boldsymbol{A}(\boldsymbol{u}, p, \xi)$ is the d'Alembert acceleration term introduced by the non-inertial transformation (3.3). The x-, y- and z-components of $\boldsymbol{A}$ are given by

$$\begin{aligned} A_x = &-\left[\frac{\partial w}{\partial t}\frac{\partial \xi}{\partial z} + w^2\frac{\partial^2\xi}{\partial z^2} + \frac{\partial\xi}{\partial z}\left(u\frac{\partial w}{\partial x} + v\frac{\partial w}{\partial y} + w\frac{\partial w}{\partial z}\right)\right] \\ &+\frac{1}{Re}\left[\frac{\partial^2}{\partial z'^2}\left(u + \frac{\partial\xi}{\partial z}w\right) - \frac{\partial^2 u}{\partial z^2} + \frac{\partial\xi}{\partial z}\nabla^2_{xy}w\right], \end{aligned} \tag{3.5}$$

$$A_y = \frac{1}{Re}\left[\frac{\partial^2 v}{\partial z'^2} - \frac{\partial^2 v}{\partial z^2}\right], \tag{3.6}$$

$$A_z = \frac{\partial\xi}{\partial z}\frac{\partial p}{\partial x} + \frac{1}{Re}\left[\frac{\partial^2 w}{\partial z'^2} - \frac{\partial^2\xi}{\partial z^2}\right]. \tag{3.7}$$

An alternative interpretation of $\boldsymbol{A}$ is as a forcing term to the flow past a straight cylinder due to the wavy geometry. As can be seen the A_x and A_z mapping terms have both inviscid and viscous parts, while the A_y term has only a viscous part. Furthermore, the inviscid mapping term of A_x contains the convective derivative of the z-component of equation (3.4). Hence by substituting the right-hand side of the z-component of equation (3.4) into the inviscid part of A_x, this mapping term can be

rewritten as

$$A_x = \left[\frac{\partial \xi}{\partial z}\left(\frac{\partial p}{\partial z}\right) - \left(\frac{\partial \xi}{\partial z}\right)^2 \frac{\partial p}{\partial x} - w^2 \frac{\partial^2 \xi}{\partial z^2}\right] + \frac{1}{Re}\left[w\frac{\partial^2}{\partial z'^2}\left(\frac{\partial \xi}{\partial z}\right) + \frac{\partial \xi}{\partial z}\left(\frac{\partial^2 \xi}{\partial z^2}\right) - \frac{\partial \xi}{\partial z}\left(\frac{\partial^2 w}{\partial z^2}\right) - \frac{\partial}{\partial z}\left(\frac{\partial \xi}{\partial z}\frac{\partial u}{\partial x}\right) - \frac{\partial \xi}{\partial z}\frac{\partial}{\partial x}\left(\frac{\partial u}{\partial z'}\right)\right]. \tag{3.8}$$

It can be appreciated that the inviscid mapping terms have two contributions from the pressure gradients in the spanwise and streamwise directions. One can write out these terms using equation (2.1) for the displacement in the ξ-direction:

$$A_{z(pressure)} = \pi \frac{W}{\lambda} \sin\left(\frac{2\pi}{\lambda} z\right) \frac{\partial p}{\partial x} \tag{3.9}$$

$$A_{x(pressure)} = \pi \frac{W}{\lambda} \sin\left(\frac{2\pi}{\lambda} z\right) \frac{\partial p}{\partial z} - \pi^2 \left(\frac{W}{\lambda}\right)^2 \sin^2\left(\frac{2\pi}{\lambda} z\right) \frac{\partial p}{\partial x} - 2w^2\pi^2 \frac{W}{\lambda^2} \cos\left(\frac{2\pi}{\lambda} z\right). \tag{3.10}$$

We therefore see that these terms depend on the wave steepness as well as the spanwise and streamwise pressure gradients which are significant near the body.

4. Results

As we have previously mentioned there is a large three-dimensional parameter space based upon Re, W/λ and λ/D. A series of computational investigations have been carried out at a Reynolds number of 100 for different values of W/λ and λ/D. All these investigations were started from a fully developed unsteady flow past a straight, non-wavy cylinder. The physical conditions can therefore be interpreted as instantaneously introducing the waviness on a straight cylinder. The flow past a straight, non-wavy cylinder is discussed in § 4.1 and can be considered as the base case to which the introduction of the waviness can be compared. In § 4.2, we will discuss the effect of the parameters W/λ and λ/D on the lift and drag forces on the body. Using the force characterization and the vortex structure identification of the wake (Jeong & Hussain 1995), we will define five distinct flow regimes in § 4.3. To illustrate these various regimes, we have focused our studies on a fixed λ/D of 5.6 and varied the parameter W/λ. In § 4.4, we summarize the regimes for a broader parametric space of $0 < \lambda/D < 11$ and $0 < W/\lambda < 0.25$. In § 4.5, we will address the influence of the initial conditions on the flow. Finally, in § 4.6, by considering the vorticity contours in the upper and lower shear layers, we introduce a physical interpretation of the length parameters W/λ and λ/D.

The wake topology is illustrated using the method proposed by Jeong & Hussain (1995). This method identifies vortical regions by locating a pressure minimum in the plane. By neglecting the influence of unsteady straining and viscous effects, they define a vortex core as a connected region containing two negative eigenvalues of $\boldsymbol{S}^2 + \boldsymbol{\Omega}^2$ (where $\boldsymbol{S}$ and $\boldsymbol{\Omega}$ are respectively the symmetric and anti-symmetric parts of the velocity gradient tensor $\nabla \boldsymbol{u}$). If $\lambda_1, \lambda_2, \lambda_3$ are the eigenvalues and $\lambda_1 > \lambda_2 > \lambda_3$, the new definition is equivalent to the requirement that $\lambda_2 < 0$ within a vortex core. A value of $\lambda_2 = -0.01$ was used to extract all the iso-surfaces in this study; vortical regions are expected to be within these iso-surfaces.

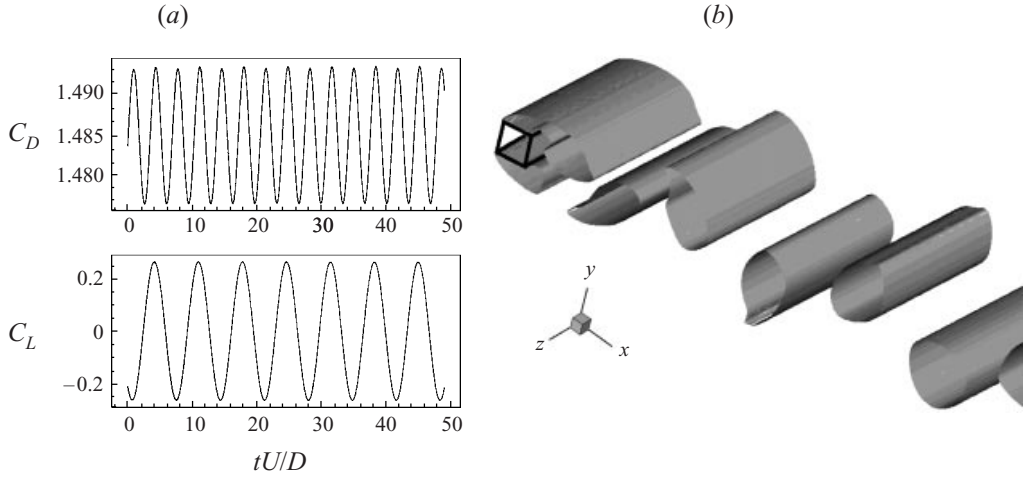

FIGURE 4. (*a*) Drag and lift coefficient history for the base case; (*b*) perspective view from above showing the two-dimensional wake at $tU/D = 42.58$ ($Re = 100$). Note that the body is shown using a wire frame.

4.1. *Straight cylinder*

A three-dimensional simulation was performed past a straight, non-wavy square-section cylinder at $Re = 100$. The spanlength of the domain was equal to $5.6D$. The time history of the lift and drag forces as well as a perspective view of the wake topology are given in figures 4(*a*) and 4(*b*), respectively. It can be clearly seen that the wake topology consists of strong spanwise vortex tubes identifying the well-known Kármán street. The values of the global flow coefficients are: $C_L' = 0.186$, $St = 0.146$ and $C_D = 1.486$.

Recent experiments reported in Sohankar, Norberg & Davidson (1998) place the critical Reynolds number for the onset of vortex shedding near $Re_c = 47 \pm 2$. Beyond this Reynolds number, the flow is unsteady and vortex shedding occurs in the near wake. An interesting flow pattern then develops on the top and bottom surfaces with increasing Reynolds number as shown in the simulations of Robichaux, Balachandar & Vanka (1999). In this work, they show that at low Reynolds numbers, the shear layers remain attached on the top and bottom surfaces. The shear layers then separate from the trailing edge, forming the Kármán vortex street in the wake. For the base case considered in this section, the shear layers always separate from the trailing edge. As the Reynolds number is increased to around $Re = 120$, the shear layers separate from the leading edge but reattach a short distance downstream, thus forming small unsteady recirculating cells on the top and bottom surfaces. Finally, at around a Reynolds number of 150, the shear layers separate from the leading edge without reattachment.

The first three-dimensional transition in the wake of a circular cylinder, referred to by Williamson (1996*b*) as mode A, occurs at a Reynolds number near $Re = 194$. Mode A appears as a waviness of the spanwise vortices with a wavelength of around 3–4 diameters and is characterized by the formation of vortex loops that connect the spanwise Kármán vortices. The formation of mode A results in a sharp drop in the Strouhal number as well as a drop in the base suction which leads to a drag reduction. As the Reynolds number is further increased the wake becomes unstable to another type of three-dimensionality known as mode B at $Re = 230$–250. This mode has

finer-scale streamwise vortices with a smaller wavelength, usually of the order of one diameter. There is now excellent agreement between computations and experimental measurements of the critical wavelength and Reynolds number (Barkley & Henderson 1996; Williamson 1996*a*, *b*). Another three-dimensional instability, mode C, has been proposed by Zhang *et al.* (1995) for $Re = 170$–270 with an intermediate wavelength of 1.8 diameters. The numerical simulations of Zhang *et al.* (1995) show that this mode C appears only in the presence of an interference wire placed close to and parallel to the cylinder axis. It therefore seems that by externally forcing the wake, other three-dimensional instabilities can be excited.

For the square-section cylinder, there is a more or less complete absence of experimental data for the transition process to three-dimensionality. On the computational side, Robichaux *et al.* (1999) performed a Floquet stability analysis (similar to the one done by Barkley & Henderson 1996) for the square-section cylinder. At a Reynolds number of 150 the wake was found to be stable to three-dimensional perturbations. They reported a long-wavelength, mode A, instability at a Reynolds number of about 160 but do not mention the associated spanwise wavelength. At a Reynolds number of 175, they found a range of unstable wavenumbers. The wavenumber with the maximum growth rate corresponds to a wavelength of 5.07 diameters. As the Reynolds number is increased to 225, three different unstable wavenumber bands are found. The first wavenumber band corresponds to the long-wavelength, mode A, with a wavelength of 5.5 diameters and the last band corresponds to mode B with a shorter wavelength of 1.2 diameters. The most amplified wavenumber for the intermediate band corresponds to a wavelength of 2.8 diameters. This wavelength was referred to as mode S in the paper. It should be noted that no precise determination of the critical values of the wavelength and Reynolds number for the onset of mode A and mode B was prescribed in this work.

In summary, the flow past a straight, non-wavy cylinder at $Re = 100$ is stable to three-dimensional perturbations and the shear layers on the top and bottom surfaces always separate at the trailing edge. The effect of introducing the spanwise waviness onto this base case will now be discussed in terms of the fluid forces and wake topology.

4.2. *Force coefficient history*

The results for the variation of the mean drag coefficient C_D and the root mean square of the total lift coefficient C_L' with respect to the wave steepness W/λ are summarized in figures 5 and 6 for values of λ/D less than and greater than 5.6, respectively. Note that the forces are normalized by the free-stream dynamic pressure and the projected area of the body to produce the drag and lift coefficients. Out of all the tests, the maximum drag reduction occurs for $\lambda/D = 5.6, W/\lambda = 0.03$ yielding a drag reduction of 16% when compared to the straight, non-wavy cylinder. It is interesting to note that for the particular case of $\lambda/D = 5.6$, the drag progressively drops until a minimum is reached at $W/\lambda = 0.03$ but then as the wave steepness is further increased the drag increases slightly. It is shown in the next section that this slight increase in drag is associated with the periodic shedding of anti-symmetric hairpin vortices from the steady near-wake region. Similar features can also be seen for $\lambda/D = 2.8,\ 4.0$. For low values of the wavelength, e.g. $\lambda/D = 1.0$, there is no substantial effect on the drag in the wave steepness range considered.

To check the results, we also performed simulations using a cylinder with two wavelengths for the cases with $\lambda/D = 2.8,\ W/\lambda = 0.09$ as well as $\lambda/D = 5.6,\ W/\lambda = 0.09$. These tests did not show any difference from a single wavelength run.

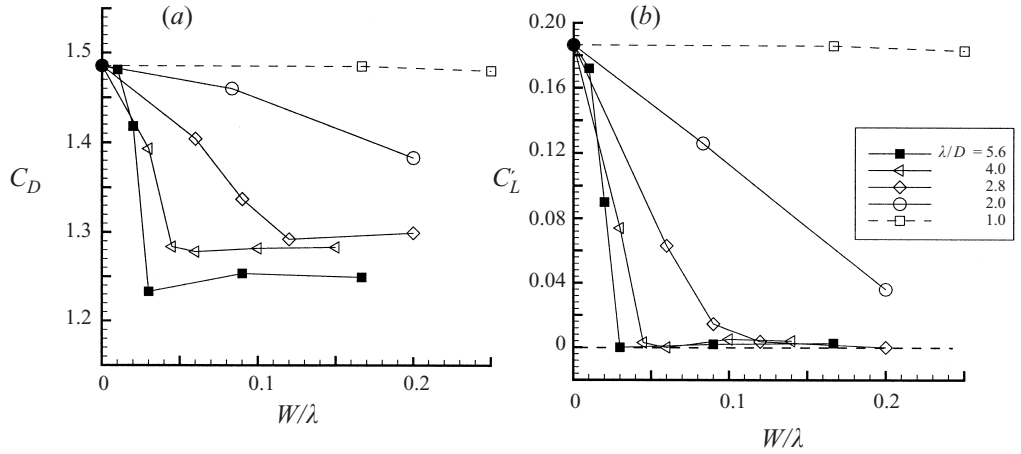

FIGURE 5. Variation of (*a*) the mean drag coefficient C_D and (*b*) the root mean square of the total lift coefficient C_L' with respect to the wave steepness W/λ for values of λ/D less than or equal to 5.6.

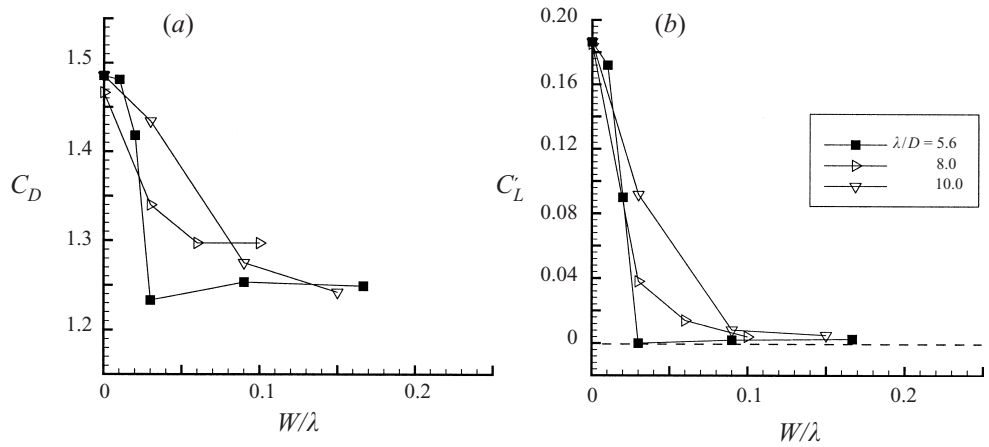

FIGURE 6. Variation of (*a*) the mean drag coefficient C_D and (*b*) the root mean square of the total lift coefficient C_L' with respect to the wave steepness W/λ for values of λ/D greater than or equal to 5.6.

The magnitude of the root mean square of the total lift coefficient C_L' is a good indicator of the level of unsteadiness and anti-symmetry present in the near-base region. As can be seen, the level of the lift force drops significantly for the $\lambda/D = 2.8, 4.0, 5.6$ cases, indicating a reduction of unsteadiness and anti-symmetry in the near-base region. C_L' is zero for three particular points ($\lambda/D = 2.8$, $W/\lambda = 0.2$), ($\lambda/D = 4.0$, $W/\lambda = 0.06$) and ($\lambda/D = 5.6$, $W/\lambda = 0.03$) which also correspond to the minimum level of the drag for each respective wavelength. Further increase in wave steepness beyond the point of zero C_L' for each wavelength results in a slight increase in the lift coefficient which is consistent with the appearance of the periodic shedding of unsteady hairpin structures to be discussed in § 4.3. For wavelengths greater than 5.6, i.e. $\lambda/D = 8$, 10 (see figure 6), the total lift coefficient drops progressively with increasing wave steepness W/λ without passing through a state where C_L' is zero. Similarly, the drag drops progressively with increasing W/λ until a minimum drag

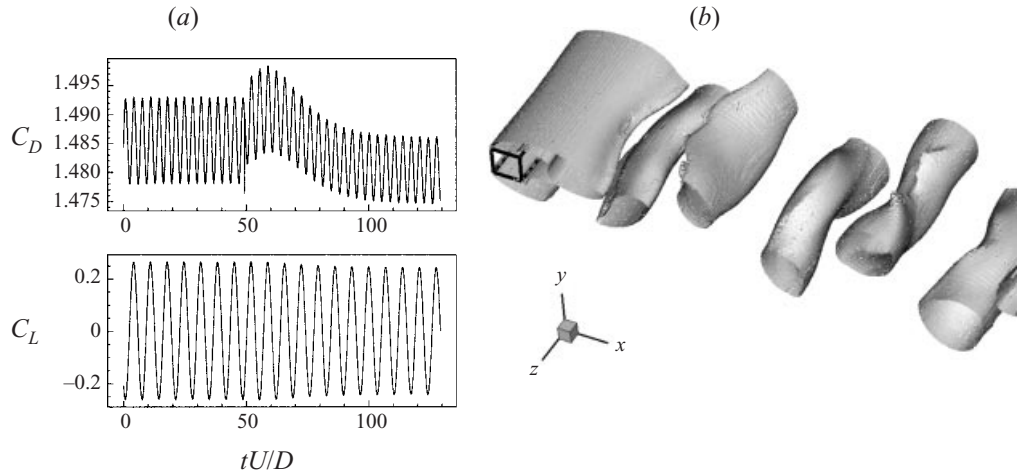

FIGURE 7. (*a*) Drag and lift coefficient history for regime I. The two-dimensional simulation without the waviness is shown until $tU/D = 49.19$, after that, the three-dimensional simulation with the waviness is shown. (*b*) Perspective view from above showing the three-dimensional wake, $tU/D = 129.19$. Note that the body is shown using a wire frame.

level is reached. In addition, it can be observed from figure 5(*b*) that at a fixed level of wave steepness W/λ, the reduction in C_L' increases as the wavelength λ/D increases from 1.0 to 5.6. However, above the critical wavelength of $\lambda/D = 5.6$, the opposite occurs, i.e at a fixed value of the wave steepness C_L' starts to increase from its minimum value at $\lambda/D = 5.6$ as the wavelength increases from $\lambda/D = 8.0$ to 10.0 (see figure 6*b*).

4.3. *Flow regimes*

Based on the previous subsection, it is clear that the flow dynamics can be classified into distinct regimes characterized by the force coefficient history. We will supplement this classification with the near-wake vortex structures. The results can be best summarized by looking at a particular wavelength and progressively increasing the wave steepness. To illustrate this, we will primarily consider the particular case of $\lambda/D = 5.6$.

4.3.1. *Regime I* – ($\lambda/D = 5.6$, $W/\lambda \approx 0$–0.015, $Re = 100$)

The spanwise waviness has a small effect on the lift and drag forces and perturbs the Kármán vortex street into a three-dimensional state (see figure 7). The unsteady and anti-symmetric shedding still occurs as can be seen from the periodicity of the lift and drag forces. The values of the global flow coefficients are: $C_L' = 0.173$, $St = 0.145$ and $C_D = 1.481$ for e.g. $W/\lambda = 0.01$. As can be seen, these values have not significantly changed (less than 3%) when compared to the base case without the waviness ($C_L' = 0.186$, $St = 0.146$ and $C_D = 1.486$). From figure 7(*b*), a three-dimensional vortex street can be seen with a small curvature appearing in the top shear layer during the formation of the Kármán vortices in the near-wake region. Further downstream, the Kármán vortices become distorted in the spanwise direction.

4.3.2. *Regime II* (*type A*) – ($\lambda/D = 5.6$, $W/\lambda \approx 0.016$–0.022, $Re = 100$)

The global flow coefficients are: $C_L' = 0.091$, $St = 0.134$ and $C_D = 1.418$ for e.g. $W/\lambda = 0.02$. As can be seen, the global flow coefficients are noticeably altered by the

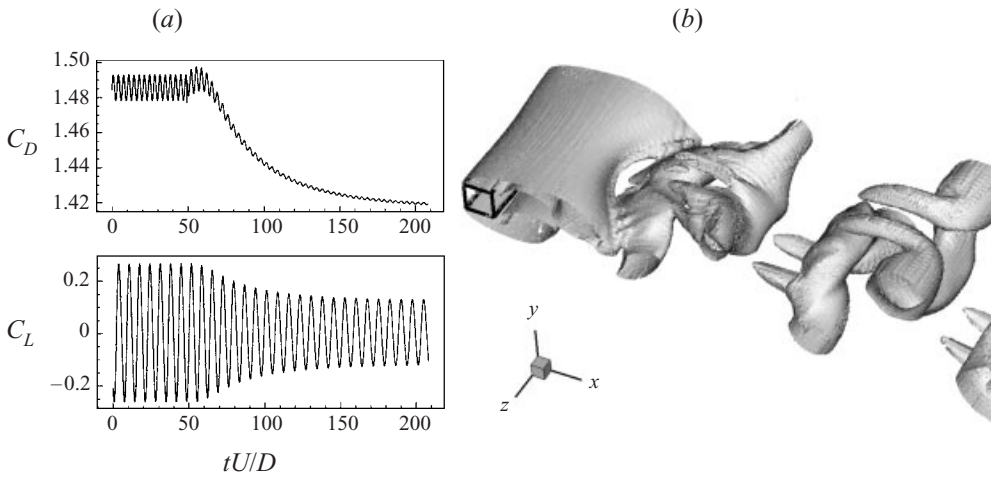

FIGURE 8. (*a*) Drag and lift coefficients history for regime II (type A). (*b*) Perspective view from above showing the three-dimensional wake, $tU/D = 208.19$.

waviness, indicating a change in the near-wake structure of the flow (see figure 8). The lift and drag have dropped by 51% and 4.5%, respectively. The shedding frequency is also reduced by 8.4%. In addition, C_D' has dropped by at least one order of magnitude. From figure 8(*b*), it can be seen that three-dimensional structures are appearing in the form of streamwise vorticity which connects adjacent spanwise vortices. Downstream of the geometric inflection points, the spanwise vortices have become highly distorted in the regions where the streamwise vorticity originates. In the formation region, there is a greater spanwise curvature of the top and bottom shear layers which leads to a direct interaction of the top shear layer and the first spanwise vortex of the bottom half of the wake (see figure 8*b*). In this case, the waviness reduces the magnitude of the forces but the near wake remains unsteady and three-dimensional with a reduced shedding frequency.

4.3.3. *Regime II* (*type B*), $Re = 100$

The previous regime II (type A), only appears when the parameter λ/D is less than or equal to about 5.6. Above this value, another type of regime II appears with a low-frequency modulation. Considering the case where $(\lambda/D, W/\lambda) = (10, 0.03)$, initially, the drag and lift drop simultaneously (see figure 9) and it is interesting to note that the lift force drops linearly in time. After this decay, the lift and drag saturate in a time-periodic state with a low-frequency modulation. The global flow coefficients are: $C_L' = 0.0917$ and $C_D = 1.434$. The low-frequency unsteadiness has a frequency of 0.01 which is approximately 1/14 of the shedding frequency of the base case (see § 4.1). From figure 9, the flow clearly seems to alternate between two distinct states. At the maximum drag and lift, the regime is mildly three-dimensional (9*b*) with a small curvature appearing in the spanwise vortices, and at the minimum drag and lift, the wake is highly three-dimensional (9*c*). This regime seems to be a combination of regime I and regime II (type A). Furthermore, a spectrum analysis of the spanwise-averaged lift force clearly demonstrates the presence of two distinct shedding frequencies as shown in figure 10. The two frequencies are 0.143 and 0.133, respectively. The higher frequency is associated with the two-dimensional shedding frequency of the base case and regime I whereas the lower frequency seems to be associated with the three-dimensional state of regime II (type A). The difference

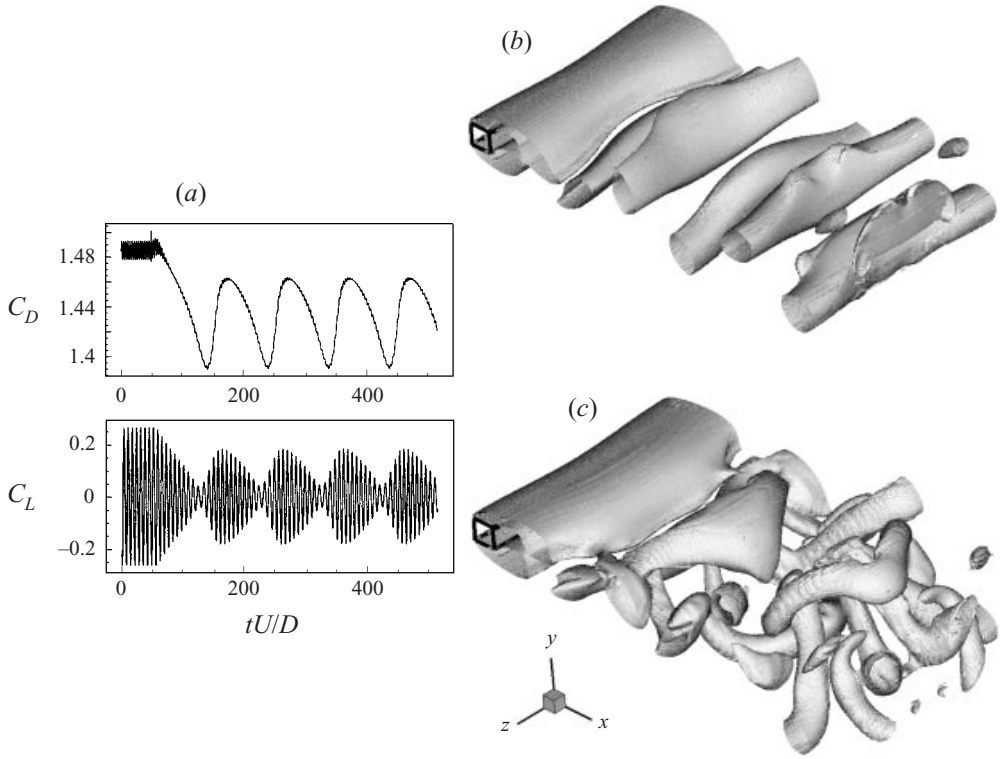

FIGURE 9. (*a*) Drag and lift coefficients history for regime II (type B) ($(\lambda/D, W/\lambda) = (10, 0.03)$). (*b*) Perspective view from above showing the vortex dynamics, $tU/D = 166.2$; (*c*) vortex dynamics, $tU/D = 244.2$.

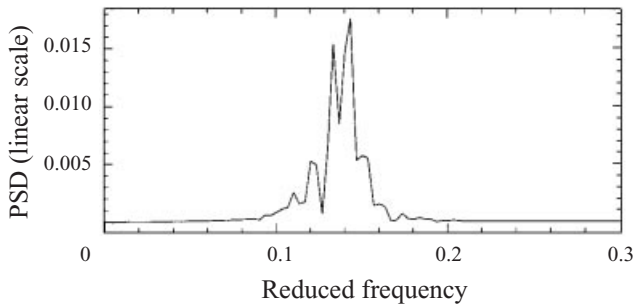

FIGURE 10. Power spectra of the spanwise-averaged lift of figure 9(*a*).

between these two frequencies, 0.143–0.133 $\approx$ 0.01, leads to the beating frequency. In figure 11 we plot the sectional lift force along the span of the wavy cylinder versus time. We see that the lift force is well correlated along the span near $tU/D = 450$ which corresponds to a maximum value of the spanwise-averaged lift force shown in figure 9(*a*). However, the correlation progressively decreases until $tU/D \approx 425$ where there is a change in phase of the sectional lift along the span. This instant in time corresponds to a minimum value of the spanwise-averaged lift force. By counting the number of black bands (corresponding to a negative peak in the lift force), it can be seen that the middle of the span is shedding at a lower frequency than the extremities.

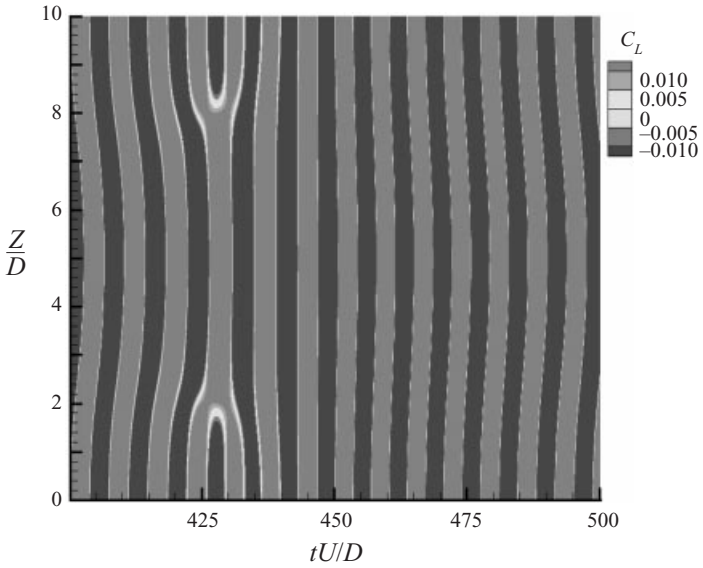

FIGURE 11. The sectional lift coefficient along the span versus time, from $tU/D = 400.2$ to 500.2, i.e. during one beating period for regime II (type B). Contour levels between 0.01 and −0.01 are used to highlight the phase difference. A maximum value of 0.25 is observed during one beating period. Note that $Z/D = 5.0$ is the minimum (most downstream cross-section) of the wavy geometry.

The middle is shedding at a frequency of 0.133 and the extremities are shedding at a higher frequency of 0.143. To accommodate the spanwise variation in the frequency of vortex shedding, we anticipate a vortex dislocation or split is occurring, leading to the phase change observed at $tU/D \approx 425$. Similar results were observed in the work of Bearman & Tombazis (1993) and Tombazis & Bearman (1997), where two main shedding frequencies were detected in the wake, resulting in the occurrence of vortex dislocations at the boundaries of the cellular vortex shedding.

4.3.4. *Regime III (type A)*–($\lambda/D = 5.6$, $W/\lambda \approx 0.023$–0.03, $Re = 100$)

The lift and drag forces drop until the lift force is zero and a time-independent state is reached (see figure 12*a*). In this saturated state, the global flow coefficients are: $C_L' = 0$, $St = 0$ and $C_D = 1.233$. The drag has hence dropped by about 16% and this is the case where the greatest reduction in drag occurs. The Strouhal frequency as well as the lift force have become zero which would suggest that the near wake has become steady. The λ_2 iso-surface is symmetric about the centreline with both vertical and horizontal connections.

4.3.5. *Regime III (type B)*–($\lambda/D = 5.6$, $W/\lambda \approx 0.04$–0.25, $Re = 100$)

The flow in the near-base region has a similar symmetry to that of regime III (type A). The global flow coefficients are: $C_L' = 0.0016$, $St = 0.082$ and $C_D = 1.245$ for $W/\lambda = 0.1667$. These values show a strong decrease in the mean drag and a drop of two orders magnitude in the lift amplitude when compared to the base case (see § 4.1). This small fluctuating lift force results in the appearance of a small unsteadiness in the near wake when compared to regime III (type A). The frequency of this unsteadiness is nearly half the shedding frequency of the cylinder without the waviness. From figure 13(*b*), it can be seen that large unsteady hairpin structures are emerging from the

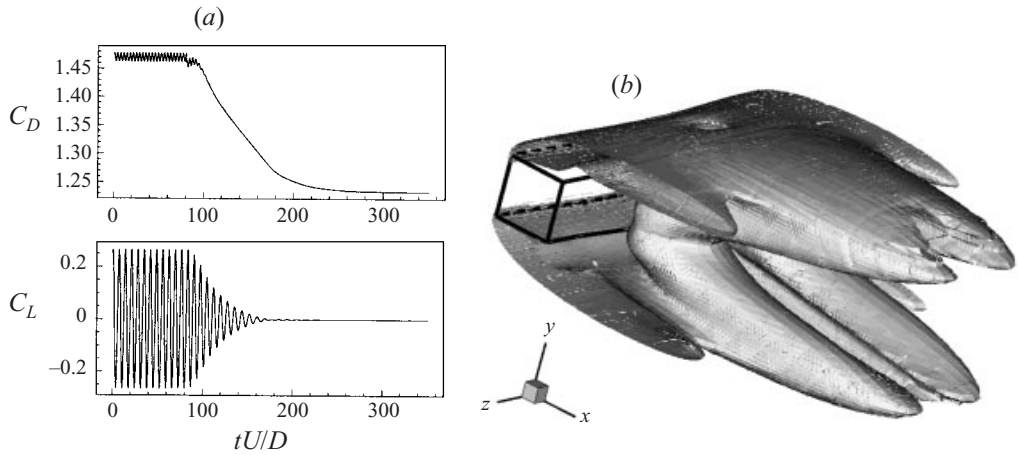

FIGURE 12. (*a*) Drag and lift coefficients history for regime III (type A). (*b*) Perspective view from above showing the vortex dynamics, $tU/D = 351$.

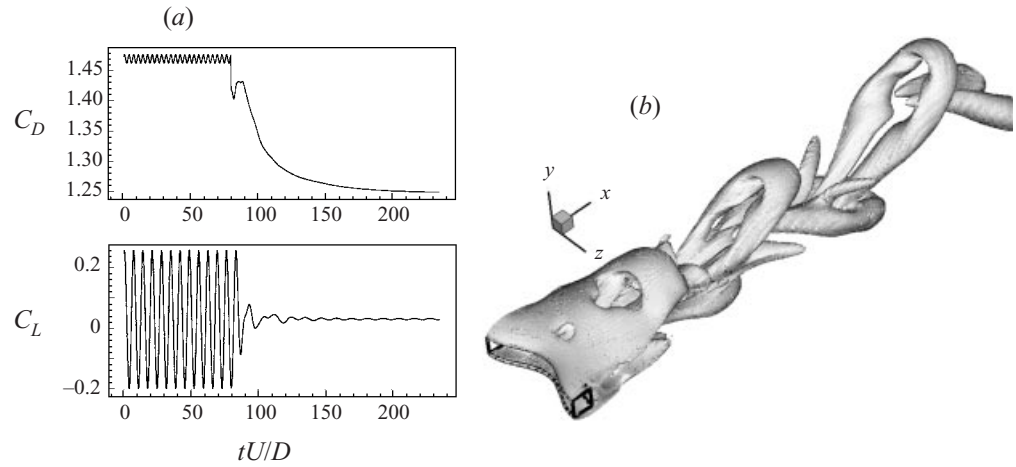

FIGURE 13. (*a*) Drag and lift coefficients history for regime III (type B). (*b*) Perspective view from above showing the vortex dynamics, $tU/D = 218$.

near-base structure observed in regime III (type A). This wake topology has similarities to the wake of a sphere at low Reynolds numbers (for example, Johnson & Patel 1999).

4.4. *Overview of the parameter space*

To obtain an overview of the simulations performed, we investigated the flow regimes for a broader parametric space $0 < \lambda/D \leqslant 10$ and $0 < W/\lambda \leqslant 0.25$ as shown in figure 14. The smallest waviness amplitude W/λ to force the flow into regime III (type A) occurs at around a critical value of $\lambda/D = 5.6$. Above this critical value, only regime II (type B) has been observed and below this critical value only regime II (type A) has been observed. In addition, below this critical value, only regime III (type A) occurs but above this value predominantly regime III (type B) has been observed with increasing values of W/λ.

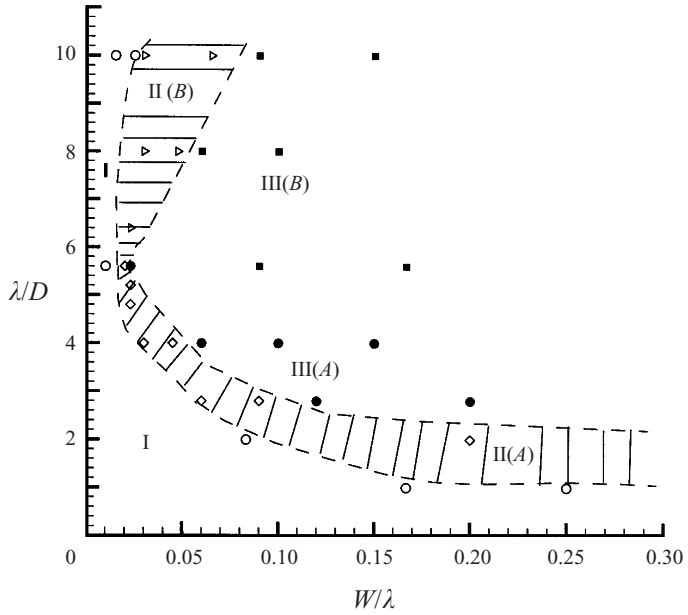

FIGURE 14. Summary of the streamwise vorticity spacing ($\sim \lambda/D$) versus the vorticity strength (W/λ) for all the cases. ○, regime I; ◇, regime II (type A); ▷, regime II (type B); ●, regime III (type A); ■, regime III (type B). The dashed region with horizontal lines denotes approximately the region where regime II (type B) occurs and the region with oblique lines is the region where regime II (type A) occurs. To the left of these two dashed regions, only regime I occurs and to the right, only regime III (type A) and regime III (type B) occur.

In summary, the flow transition as W/λ is increased for a fixed λ/D can be viewed as

$$\text{regime I} \Rightarrow \text{regime II (type A or B)} \Rightarrow \text{regime III (type A or B)}$$

In regime I, a small curvature appears in the top and bottom shear layers during the formation of the Kármán vortices in the near-wake region. Further downstream, there is a discernible spanwise deformation of the Kármán vortices. Regime II is the unsteady transitional regime where the three-dimensional effects are more dominant in the formation region. A large spanwise curvature appears in the top and bottom shear layers. Further downstream streamwise vortices associated with the sinusoidal spanwise deformation of the distorted Kármán vortices are observed. Within regime II, there is a further distinction between normalized wavelengths above and below $\lambda/D \approx 5.6$. For $\lambda/D \leqslant 5.6$, denoted as regime II (type A), a time-periodic state with a single frequency is observed. However, for $\lambda/D > 5.6$ denoted as regime II (type B), we observe a beating phenomenon where the wake topology alternates between a mildly three-dimensional state similar to regime I and a highly three-dimensional state similar to regime II (type A). Finally, for a sufficiently large waviness amplitude, the near-base region is steady and the Kármán vortex street is suppressed. This regime is defined as regime III (type A) and it is in this regime that the greatest reduction in drag occurs. It was shown that the smallest waviness W/λ to force the flow into regime III (type A) occurs at around a critical wavelength of $\lambda/D = 5.6$. However, for $\lambda/D \geqslant 5.6$ with higher waviness amplitudes, hairpin vortices are emerging periodically from the near-base region. In this regime, defined as regime III (type B), a small unsteadiness appears in the near wake due to the shedding of these hairpin vortices.

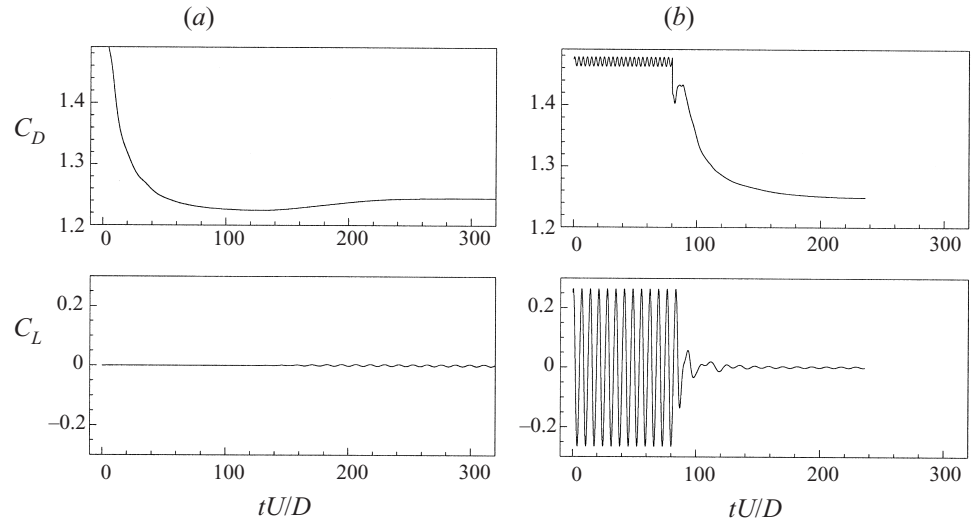

FIGURE 15. Comparison of the lift and drag coefficient history for the two different initial conditions. (*a*) Initial conditions: wavy cylinder started with free-stream conditions (note that in this case the plot is shown from $tU/D = 10$); (*b*) initial conditions: two-dimensional shedding, the restart with the waviness is done at $tU/D = 80$.

While the λ/D axis represents the straight, non-wavy cylinder, the axis W/λ is not easily interpreted physically since by definition along this axis $\lambda/D = 0$ making W/λ infinite for any finite W and D. However, if we consider the case where $\lambda/D = \epsilon$ where $\epsilon \ll D$ then we expect the waviness to have a minimal effect since the wavelength of the oscillation will be much lower than any other scale in the problem, especially since we have limited our observations to $W/\lambda \leqslant 0.25$.

4.5. *Effect of initial conditions*

Observations from on-going experiments of wavy cylinders by J. C. Owen & P. W. Bearman (private communication, 1999) have raised the issue of the effect of the initial conditions on the wake structure. To investigate this point, two different initial conditions for the case of $\lambda/D = 6.0$, $W/\lambda = 0.1667$ were used. In the first case, the simulation was started from $tU/D = 0$ past a wavy cylinder with uniform free-stream conditions, i.e. $(u, v, w) = (1, 0, 0)$. In the second case, the waviness was instantaneously applied to the unsteady flow past a square-section cylinder without the waviness, i.e. the base case (see § 4.1). In both cases, the force history was monitored over time and the vortex structures extracted at particular instances in time for comparison. Note that for the second set, slightly different length parameters were used, $\lambda/D = 5.6$, $W/\lambda = 0.1667$. The lift and drag coefficient history for both cases is shown in figure 15. In the first case, the lift is zero for approximately 60 time units but then grows until it saturates in a time-periodic state. In this saturated state, the values for the global parameters are: $C_L' = 0.0017$, $St = 0.085$ and $C_D = 1.244$. The lift amplitude is hence very small, two orders of magnitude less, than the amplitude of the lift without the waviness present (see § 4.1). Vortex structures were extracted at $tU/D = 56.25$ when the lift is zero and $tU/D = 303.75$, when the lift has saturated in a time-dependent state. The results are shown in figure 16. It is interesting to see that during the transient time when the lift is zero, the wake is symmetric about the centreline and is formed of periodic hairpin structures being shed from the near-

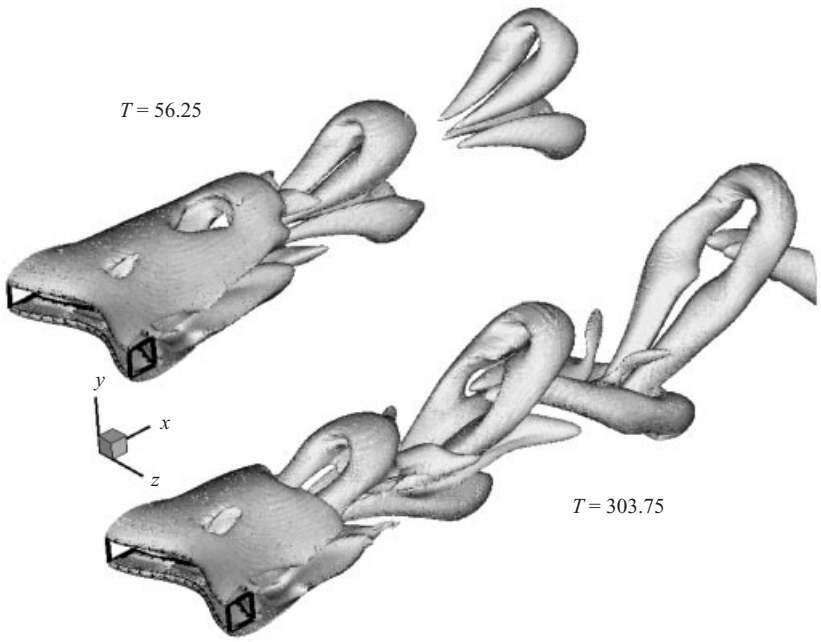

FIGURE 16. Perspective view of the vortex structure in the wake at two different times illustrating the breaking of the symmetry about the centreline. At $tU/D = 56.25$, the hairpin structures are symmetric during a transient phase but then the flow saturates in a time-dependent state where the hairpin structures are anti-symmetric ($tU/D = 303.75$).

wake region. After a long transient time, the shedding becomes anti-symmetric which results in the oscillatory behaviour of the lift coefficient history. The force history for the second initial conditions where the waviness was instantaneously applied to fully developed shedding past a non-wavy cylinder is shown in figure 15(*b*) and indicates a rapid decay in the lift coefficient although small oscillations are still present at long times. At saturation, the values for the global coefficients are: $C'_L = 0.0016$, $St = 0.082$ and $C_D = 1.245$. These values are in good agreement with the data obtained when the simulation was started at $tU/D = 0$. The vortex structure has been extracted at $tU/D = 218$ (see figure 13*b*) and is in agreement with figure 16 at $tU/D = 303.75$, where the wake is also anti-symmetric.

We therefore believe that at $Re = 100$ the initial conditions do not alter the asymptotic state of the simulation but do influence the vortex dynamics over a long transient time period before the flow saturates. Unless otherwise stated, all simulations have been restarted from the unsteady flow past a straight, non-wavy body.

4.6. *Interpretation of the λ/D and W/λ parameters*

To investigate the physical interpretation of the length parameters λ/D and W/λ, contours of each of the vorticity components in a (y, z)-plane normal to the flow at $x = 0$ have been extracted for regime III (type A) for the particular case $(\lambda/D, W/\lambda) = (5.6, 0.03)$ at $tU/D = 351$ (when the lift force is zero) and are shown in figure 17. This plane is of importance because the shear layers have not yet reached the near-wake region. Contours of ω_z are drawn for levels of 0.8, 2.4, 4.0, 4.8 with the zero contour omitted for clarity and negative values drawn with dashed lines. Similarly, in figure 17(*b*, *c*), we have plotted ω_x and ω_y contours for increments of 0.04 and 0.00675, respectively. It can be seen, that there is already a presence of streamwise and vertical vorticity within

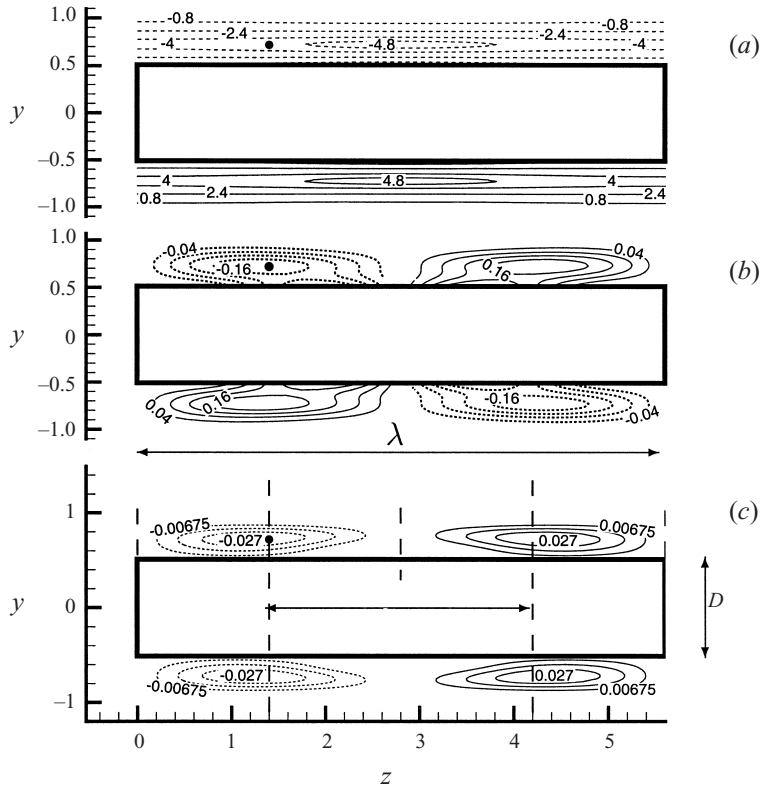

FIGURE 17. Contours of vorticity in a vertical plane at $x = 0$: (*a*) contours of ω_z; (*b*) contours of ω_x and (*c*) contours of ω_y. The black dot on the left of all plots denotes the location of the survey point used to measure the strength of the different components of vorticity with increasing wave steepness W/λ (see figure 18).

the shear layers which does not appear in the base case, i.e. for the straight cylinder at $Re = 100$. There is a spanwise variation in the levels of ω_z, which has a value of 4.8 at the valley and decays to 4.0 at the peaks (see figure 17*a*). This spanwise variation of ω_z occurs mainly in the region of the inflection points and leads to the appearance of the extra components of vorticity ω_x and ω_y. These extra components of vorticity appear in organized elliptical regions which are aligned with the position of the geometric inflection points. Hence, the ratio of the spanwise to vertical spacing of these additional ω_x and ω_y vorticity components is equal to half the geometric wavelength, i.e $\frac{1}{2}\lambda/D$.

Furthermore, the strength of these extra components of vorticity was investigated by probing the values of ω_x/ω_z and ω_y/ω_z in the same (y, z)-plane at a z value corresponding to the inflection points and a y value within the shear layers, i.e. at $(z, y) = (1.4, 0.72)$. This point is shown as a black dot on figure 17(*a–c*). These values were extracted as a function of the wave steepness W/λ for a fixed $\lambda/D = 5.6$ and are shown in figure 18. Beyond a value of $W/\lambda = 0.03$ when the near wake becomes steady, we observe an almost linear increase in ω_x/ω_z while ω_y/ω_z seems to saturate for high W/λ. In addition, the values of ω_x/ω_z are approximately an order of magnitude greater than those of ω_y/ω_z.

We note that the predominant feature of the waviness is to modify the spanwise distribution of ω_z within the top and bottom shear layers. The spanwise variation

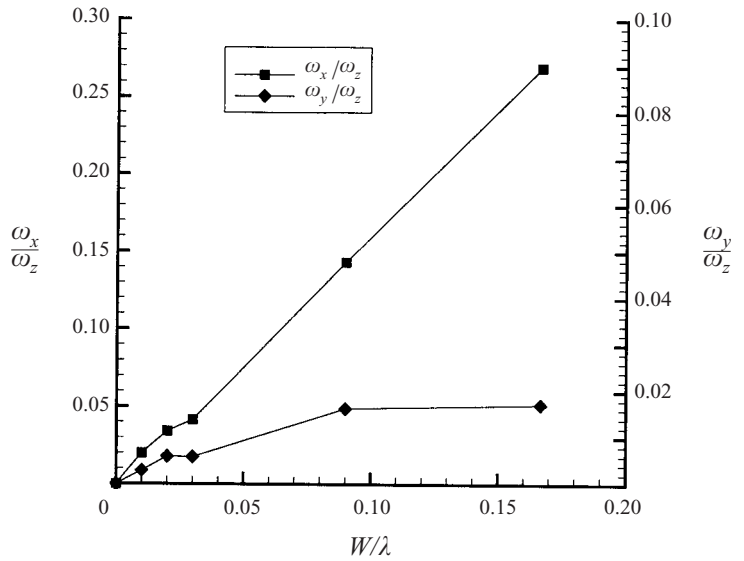

FIGURE 18. Variation of ω_x/ω_z and ω_y/ω_z with increasing wave steepness W/λ for $\lambda/D = 5.6$.

leads to the appearance of mainly streamwise vorticity ω_x in the top and bottom shear layers. This streamwise component of vorticity appears in the region of the geometric inflection points with a spanwise spacing equal to $\frac{1}{2}\lambda/D$. In addition, the strength of ω_x increases with increasing wave steepness W/λ. Based on these observations, we introduce the following physical interpretation for the length parameters:

(*a*) λ/D: ratio of the *spanwise* to *vertical* spacing of the streamwise vorticity;

(*b*) W/λ: wave steepness which governs the strength of the streamwise vorticity.

5. Discussion

In the earlier work of Bearman & Tombazis (1993) and Tombazis & Bearman (1997), the wake past a body with wavy trailing edge was studied at a Reynolds number of 40 000. Vortex shedding was found to occur up to a wave steepness of 0.14 with an associated drag reduction of 34%. Two main shedding frequencies were detected in the wake, which resulted in the occurrence of vortex dislocations at the boundaries of the cellular vortex shedding. A similar wake pattern is observed in regime II (type B) of the present study, where a low-frequency beating occurs due to two distinct shedding frequencies. Lasheras & Choi (1988), Meiburg & Lasheras (1988) and Lasheras & Meiburg (1990) carried out experiments on and simulations of the three-dimensional structure of the wake at moderate Reynolds numbers (≈ 100) behind a flat plate subjected to periodic spanwise perturbations. They introduced a sinusoidal streamwise and vertical undulation at the trailing edge of the plate and observed qualitatively the transition process by studying the evolution of the interface that separates the two streams composing the wake. They found that these spanwise perturbations resulted in the formation of counter-rotating pairs of streamwise vortex tubes that are located in the braids, connecting consecutive Kármán vortices of opposite sign. These streamwise structures have some analogy to the ones found in the three-dimensional wake transition of a circular cylinder (modes A and B), see Williamson (1996*a*). In the present study, regime II (type A) where streamwise vorticity is observed in the braid region

connecting opposite sign vortices, has similarities with mode A and the streamwise structures found in the work of Lasheras & Meiburg (1990) and co-workers.

In these two bodies of work, the waviness was introduced at the trailing edge of the body and the primary instability (Kármán vortex shedding) was not suppressed. It seems that in one case, the wavy trailing edge forced vortex dislocations and in the second, forced earlier transition to a three-dimensional wake by producing streamwise vortices in the braids that connect adjacent Kármán vortices. Both of these effects have been reproduced, in the present study, for the wavy-leading-edge bodies.

Regime II (type A) corresponds to the case where streamwise vortices connect adjacent Kármán vortices and regime II (type B) to the case where a beating occurs due to two distinct frequencies in the wake. We assume that there is a similar pattern of vortex dislocations to that reported in Bearman & Tombazis (1993) and Tombazis & Bearman (1997). However, for the wavy-leading-edge bodies, further increase in the amplitude of the waviness leads to the complete suppression of the primary instability (Kármán vortex shedding), which does not occur for the wavy-trailing-edge bodies. The wavy-leading-edge bodies introduce three-dimensional effects much earlier during the shedding process than the wavy-trailing-edge bodies, which makes the former bodies more sensitive to wave steepness. These three-dimensional effects redistribute the vorticity within the growing boundary layer on the wavy stagnation face and subsequent shear layers on the top and bottom surfaces. On the other hand, for the wavy-trailing-edge bodies, the boundary layer and shear layers are still two-dimensional until the shear layers separate from the wavy trailing edge. In order to demonstrate why the wavy-leading-edge body is capable of suppressing the primary instability, the results will be discussed mainly for regime III, which is the steady regime and the case where most drag reduction occurs.

From the results section, it is clear that the introduction of the spanwise waviness on the stagnation face has significantly influenced the overall forces and wake characteristics of the base case, i.e. the straight, non-wavy cylinder. The main observations made during the present numerical simulations and the experiments (Bearman & Owen 1998*a*, *b*) can be summarized into the following main points:

significant drag and lift reductions are observed in regime III (type A or B);
near-wake width variation across the span;
large-scale recirculating cells along the span in the near-base region in regime III (type A or B);
loss of the Strouhal frequency in the wake for regime III (type A or B).

Each of these specific characteristics will be now addressed with emphasis on regime III (type A or B) where the most significant reduction in drag occurs.

5.1. *Reduction in drag*

The progressive reduction in drag observed in the successive flow regimes is mainly due to the increase in the mean level of the static pressure in the near-base region, i.e. the mean base pressure. The base pressure is highest in regime III (type A) where most of the drag reduction occurs. The increase of the mean base pressure can be associated with the fact that the near-base region becomes steady. This can be seen from the force history where the fluctuating components of the lift C_L' and drag C_D' drop to nearly zero in regime III (type A or B) (see figures 5 and 6). The steady and unsteady drag curves for the square cylinder are plotted in figure 19 and clearly show the reduction in drag associated with the steady branch. However, at low Reynolds numbers ($Re = 10$ and 30), the drag level of the wavy cylinder is similar to that of the

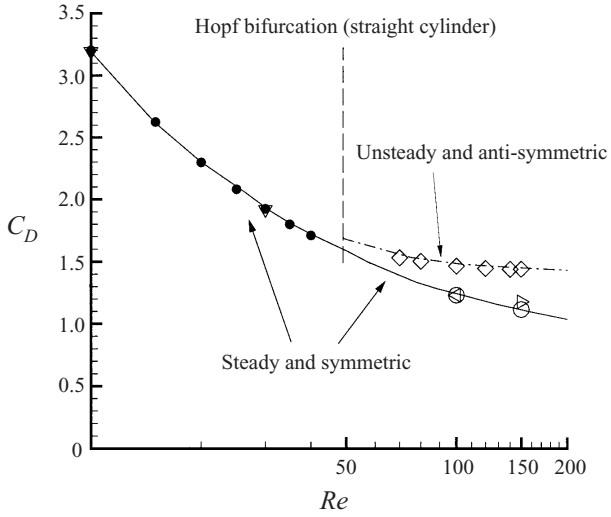

FIGURE 19. Unsteady and steady drag curves as a function of Re for the flow past a straight and wavy square-section cylinder. •, two-dimensional steady simulations for the straight cylinder at $Re = 10, 15, 20, 25, 30, 35$ and 40; ◇, two-dimensional unsteady simulation for the straight cylinder at $Re = 70, 80, 100, 120, 140$ and 150; ○, two-dimensional *steady* simulation for the straight cylinder at $Re = 100, 150$; ◁, wavy cylinder (regime III (type A)) at $Re = 100$; ▷, wavy cylinder (regime III (type B)) at $Re = 150$; ▽, wavy cylinder at $Re = 10$ and 30.

non-wavy cylinder. Note that to obtain a steady flow past the non-wavy cylinder at $Re = 100$, symmetry may be imposed using half of the mesh shown in figure 26(*a*) in the Appendix with symmetry boundary conditions $v = 0$, $\partial u/\partial n = 0$ on the centreline.

A reduction in the fluctuating forces or the velocity fluctuations in the near-base region is usually associated with an increase in the mean base pressure as was shown in experiments using splitter plates (Roshko 1955; Bearman 1965) and base bleed (Bearman 1967). The splitter plate and base bleed stabilize the near wake by delaying the interaction of the top and bottom shear layers in the near wake and hence suppress the formation of low-pressure vortices associated with the unsteady Kármán vortex wake. The suppression of these low-pressure vortices in the near-base region leads to an increase in the mean base pressure and hence results in a drag reduction. The increase in base pressure can be seen from the surface pressure coefficient C_P plots shown in figure 20. The pressure coefficient is defined as $C_P \equiv (p - p_\infty)/\frac{1}{2}\rho U_\infty^2$, where p is the time-averaged pressure and p_∞ is the static pressure at infinity. Note that the fast pressure recovery on the side BC is due to the fact that the shear layers do not separate from the leading edge B at $Re = 100$ (see § 4.1).

As can be seen, there is an increase in the base pressure on the side CD for the simulation with the splitter plate (of length, $l \approx 7D$) where the near wake has been stabilized. Similar results are also obtained in regime III (type A) which would suggest that the waviness in regime III is strong enough to delay the top and bottom shear layers from interacting and hence suppress the formation of the low-pressure vortices in the near wake.

5.2. *The A_z and A_x forcing terms*

We recall from § 3.1 that another way of interpreting the effect of the geometric waviness is the addition of inviscid and viscous forcing terms in the momentum equation for a straight cylinder. The A_x and A_z mapping terms have both inviscid

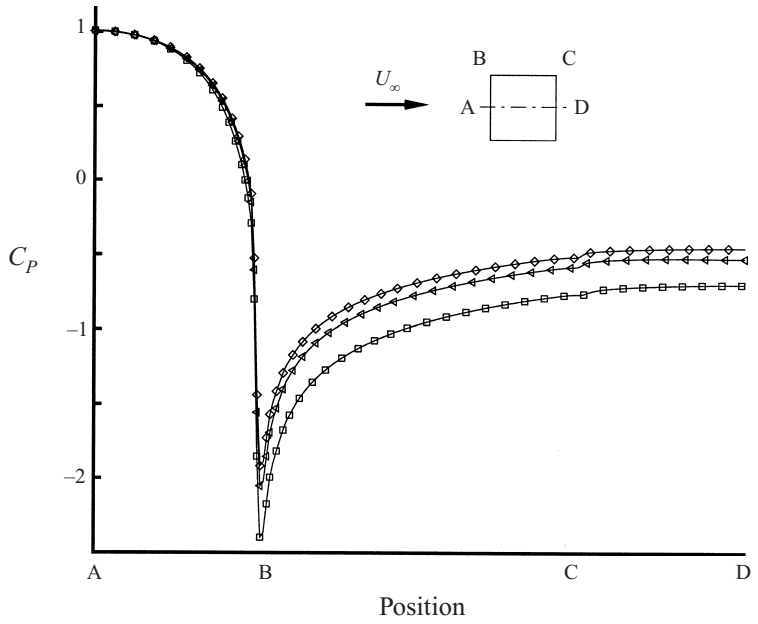

FIGURE 20. Comparison of the surface pressure distribution C_P around the body for three cases: □, non-wavy cylinder; ◁, non-wavy cylinder with a splitter plate of length $l \approx 7D$; ◇, wavy cylinder (regime III (type A)).

and viscous parts, while the A_y term has only a viscous part. Simulations were performed neglecting the viscous terms and no significant differences (less than 1%) were observed in the forces or the wake topology when compared to the simulations with the full forcing terms. The forcing terms can therefore be modelled as

$$A_x = \pi \frac{W}{\lambda} \sin\left(\frac{2\pi}{\lambda} z\right) \frac{\partial p}{\partial z} - \pi^2 \left(\frac{W}{\lambda}\right)^2 \sin^2\left(\frac{2\pi}{\lambda} z\right) \frac{\partial p}{\partial x} - 2w^2 \pi^2 \frac{W}{\lambda^2} \cos\left(\frac{2\pi}{\lambda} z\right), \quad (5.1)$$

$$A_y = 0, \quad (5.2)$$

$$A_z = \pi \frac{W}{\lambda} \sin\left(\frac{2\pi}{\lambda} z\right) \frac{\partial p}{\partial x}. \quad (5.3)$$

These inviscid forcing terms depend mainly on the spanwise and streamwise pressure gradients. The A_z term, given by equation (5.3), depends on the streamwise pressure gradient and the z-derivative of the shape of the waviness. The streamwise pressure gradient $\partial p/\partial x$ will be large near the stagnation face and will always be positive. The forcing term A_z will therefore be positive between $0 < z < \lambda/2$ and negative between $\lambda/2 < z < \lambda$ as illustrated in figure 21(*a*).

This forcing therefore sets up a spanwise or cross-flow velocity component, w, along the leading-edge surface going from a position corresponding to the maximum towards a position corresponding to the minimum of the wavy cylinder. The spanwise component w of the velocity along the leading-edge surface reaches 3%, 5% and 20% of the free-stream velocity with increasing values of W/λ for regime II (type A), III (type A) and III (type B), respectively. The spanwise component w will result in a spanwise pressure gradient, $\partial p/\partial z$, along the leading-edge surface. This spanwise pressure gradient as well as the streamwise pressure gradient, $\partial p/\partial x$, contribute to the streamwise forcing term, A_x. From equation (5.1), there are two terms which depend

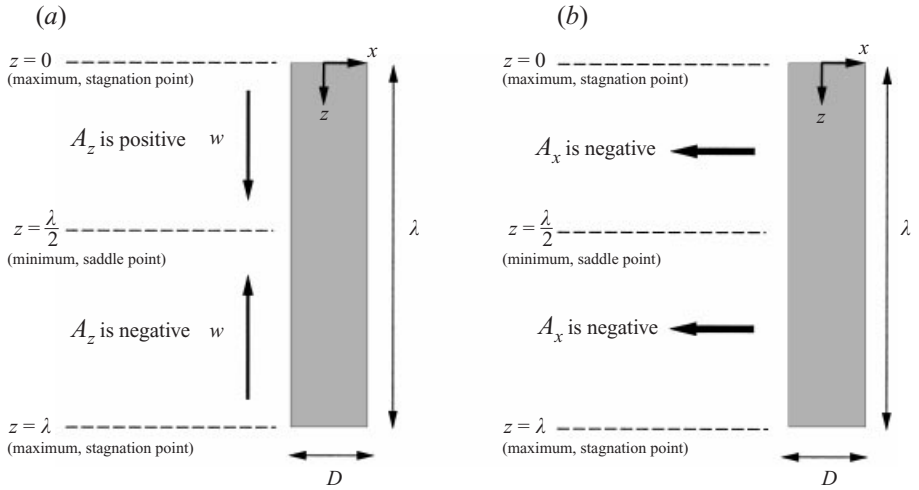

FIGURE 21. (*a*) Schematic of the d'Alembert forcing term A_z in the spanwise component of the momentum equation. This forcing term is positive in one half of the domain and negative in the other, thus setting up a cross-flow w, corresponding to the flow from the maximum to the minimum in the wavy cylinder. (*b*) Schematic of the A_x forcing term which is negative in the region of the inflection points thus slowing down the u-component of the velocity.

on the pressure gradients:

$$\pi\frac{W}{\lambda}\sin\left(\frac{2\pi}{\lambda}z\right)\frac{1}{\rho}\frac{\partial p}{\partial z}-\pi^2\left(\frac{W}{\lambda}\right)^2\sin^2\left(\frac{2\pi}{\lambda}z\right)\frac{1}{\rho}\frac{\partial p}{\partial x}$$

and a term which depends on the cross-flow component w, i.e.

$$-2w^2\pi^2\frac{W}{\lambda^2}\cos\left(\frac{2\pi}{\lambda}z\right).$$

The latter term is typically negligible since the maximum value of w is close to 0.2, making $-2w^2\pi^2W/\lambda^2$ at least one order of magnitude less than the leading coefficients of the pressure gradient terms. By comparing the sign of the two pressure gradient terms, we see that they both contribute to a net negative forcing in the region close to the leading edge. A closer inspection of the magnitude of the forcing term A_x revealed that it reaches a negative peak near the inflection points. This latter observation can also be inferred from the fact that the streamwise pressure gradient is larger than the spanwise pressure gradient at the leading-edge surface. Hence, the A_x forcing term is mainly dominated by

$$-\pi^2\left(\frac{W}{\lambda}\right)^2\sin^2\left(\frac{2\pi}{\lambda}z\right)\frac{1}{\rho}\frac{\partial p}{\partial x}$$

which is negative all along at the leading edge and reaches a maximum in the region of the inflection points as shown in figure 21(*b*). The streamwise forcing term, A_x, will thus slow down the two-dimensional u component of the velocity more significantly close to the inflection points, which is consistent with the cross-flow w reaching a maximum in that region. In addition, we found that near the stagnation face the magnitude of the A_z forcing term is at least 70% greater than the magnitude of the A_x forcing term.

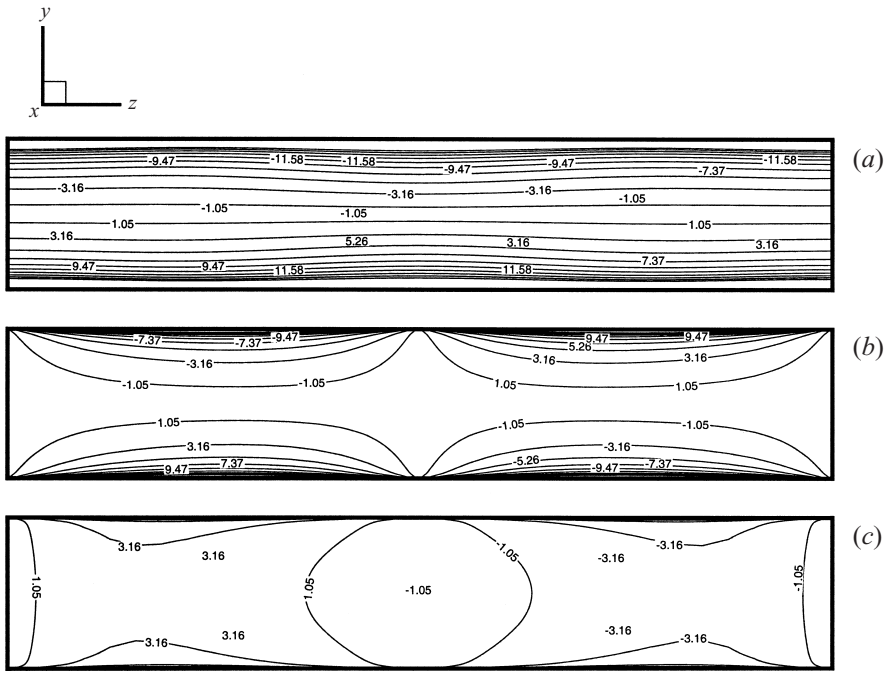

FIGURE 22. Contours of the vorticity components on the wavy leading edge surface ($\lambda/D = 5.6$, $W/\lambda = 0.1667$). (*a*) ω_z; (*b*) ω_x; (*c*) ω_y.

5.3. *Cross-flow*

The cross-flow component at the leading-edge surface is present in all flow regimes. It is small in regime I and II but reaches a maximum of 5% and 20% of the free-stream velocity in regime III (type A) and regime III (type B), respectively. The effect of the cross-flow at the leading-edge surface is twofold.

First, in addition to the usual spanwise vorticity component $\omega_z = (\partial v/\partial x - \partial u/\partial y)$ within the growing boundary layer, the cross-flow will generate a vertical component of the vorticity $\omega_y = (\partial u/\partial z - \partial \omega/\partial x)$ as well as a streamwise component $\omega_x = (\partial \omega/\partial y - \partial v/\partial z)$. These extra components of vorticity, ω_x and ω_y are shown in figure 22. From a quantitative analysis, it was found that only the spanwise derivatives $\partial v/\partial z$ and $\partial u/\partial z$ dominate ω_x and ω_y, respectively. The origin of the streamwise and vertical components of vorticity can therefore be attributed to the rate of change of the two-dimensional velocity components u and v in the spanwise direction.

Secondly, the cross-flow will lead to a higher influx of spanwise velocity w near the saddle point (minimum) which will then result in a higher vertical velocity v within the shear layers than in the region of the stagnation point (maximum). A spanwise gradient of v will hence result within the top and bottom shear layers, which is consistent with the appearance of the streamwise vorticity, ω_x.

5.4. *Near-wake width variation across the span*

During experiments (Bearman & Owen 1998*a*, *b*) and the present numerical simulations, a wake width variation was observed along the span of the wavy cylinder. This is illustrated for the present numerical simulations in figure 23. The wake is wide behind the minimum and narrow behind the maximum. This three-dimensionality of the near wake is consistent with the appearance of the streamwise vorticity and the

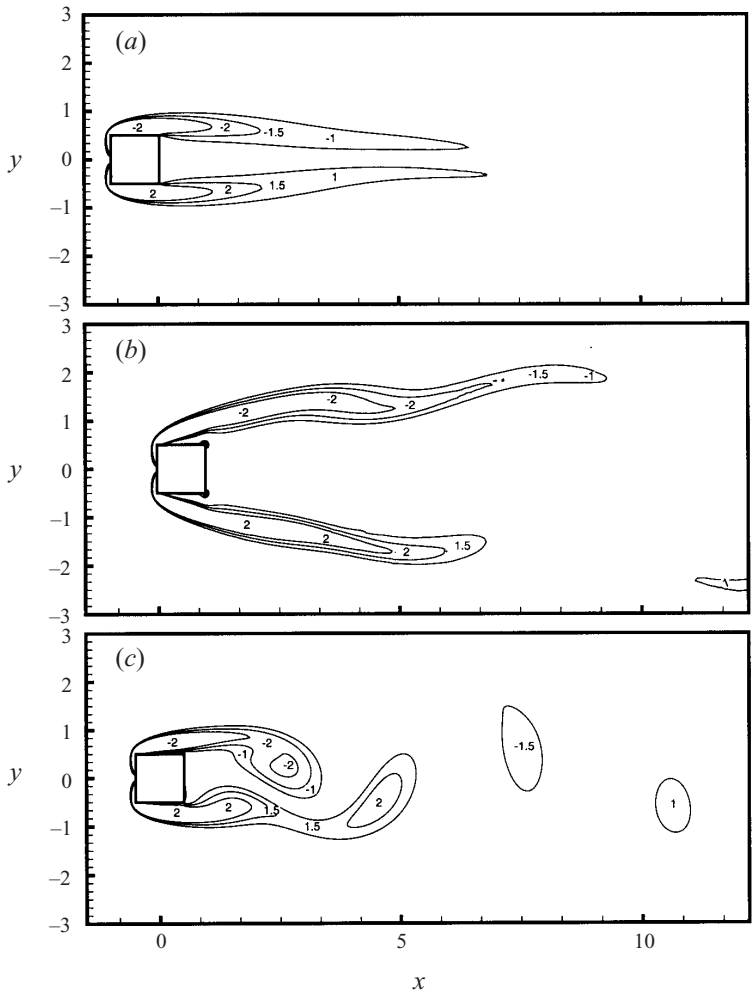

FIGURE 23. Instantaneous spanwise vorticity ω_z contours for regime III (type B) at (*a*) the maximum $z = 0$ and (*b*) minimum $z = 2.8$ cross-sections showing the variation of the wake width along the span (total spanlength equals 5.6*D*). For comparison, the instantaneous contours for the non-wavy cylinder are also shown in (*c*).

change in the vertical velocity distribution within the top and bottom shear layers as shown schematically in figure 24. The streamwise vorticity creates an upwash behind the maximum and a downwash behind the minimum which displace the near wake in a sinusoidal fashion. The variation of the vertical velocity field v within the shear layers will also contribute to the widening and narrowing of the near wake by pushing the free shear layers further apart in the vertical direction behind the minimum where the v velocity component is maximum. This three-dimensionality of the shear layers is associated with the earlier separation of the shear layer just after the leading edge at the minimum (see figure 23*b*), while at the maximum the shear layer remains attached as in the base case (see figure 23*a*, *c*).

The change in wake width along the span is also associated with a three-dimensional distribution of the static pressure in the near-base region. This three-dimensional distribution can be seen from the time-averaged pressure coefficients C_P in the

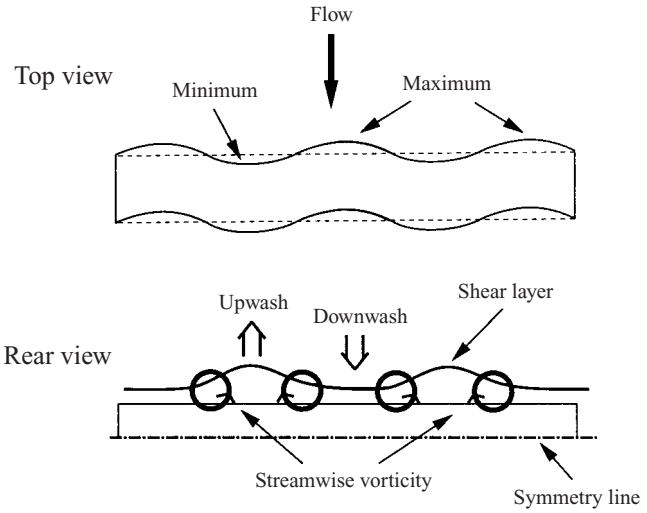

FIGURE 24. Schematic view of the relation between the streamwise vorticity and wake width variation along the span.

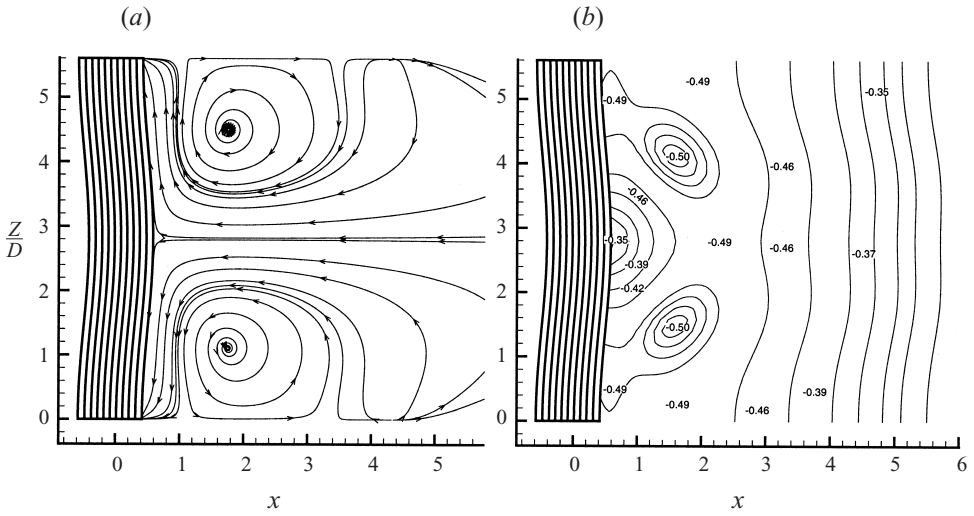

FIGURE 25. (*a*) Centreplane $y = 0$ streamlines showing the two recirculating cells in the near-base region for regime III (type A); (*b*) time-averaged pressure coefficient C_P contours at $y = 0$ for regime III (type A).

centreplane $y = 0$ for regime III (type A), shown in figure 25(*b*). It can be observed that the static pressure is higher at the minimum and lower at the maximum in the near-base region. For example, the difference is $C_{P_{min}} - C_{P_{max}} = \Delta C_P \approx 0.14$ near the backface for regime III (type A). For regime III (type B) $\Delta C_P \approx 0.12$ and for the other regimes, ΔC_P is less than 0.09.

A pressure gradient is therefore produced from the minimum to the maximum in the near-base region which leads us to the next physical observation of the recirculating cells.

5.5. *Recirculating cells*

Two recirculating cells have been observed in the near-base region for regime II and III. These cells are shown in figure 25(*a*) for more clarity using two-dimensional streamlines in the centreplane for regime III (type A). These cells are aligned with the inflection points and have also been reported in on-going experiments (J. C. Owen & P. W. Bearman, private communications 1999). The maximum spanwise velocity w attained in these cells reaches 10%, 19% and 20% of the free-stream velocity with increasing values of W/λ for regimes II (type A), III (type A) and III (type B), respectively. The progressive increase in strength of these recirculating cells leads to the appearance of two local pressure minima in the near-base region at $x \approx 1.8$ for regime III (type A or B) only, as can be seen from the pressure coefficient plot shown in figure 25(*b*).

The appearance of the recirculating cells is clearly consistent with the existence of the spanwise pressure gradient in the near-base region mentioned in the previous section. A potential driving force for the recirculating cells results from the wake width variation which is observed to produce a near-base pressure gradient.

5.6. *Suppression of the Kármán vortex shedding*

It was shown in §§ 4.6 and 5.3, that the top and bottom shear layers have a spanwise variation in the level of ω_z, which leads to the appearance of additional components of vorticity ω_x and ω_y in the region of the geometric inflection points. This additional vorticity, particularly the ω_x component, tends to distort the two-dimensional ω_z shear layers so that they are pushed further apart in the vertical direction behind the minimum as shown in figures 23 and 24. It would seem reasonable that the suppression of the Kármán vortex shedding can be attributed to the development of the three-dimensional shear layers making them less susceptible to rolling-up into a Kármán vortex street by diverting spanwise vorticity into streamwise and vertical components of vorticity. This three-dimensional redistribution of vorticity within the boundary layer and shear layers may prevent the shear layers interacting in the near-base region and hence suppress the Kármán vortex shedding. In contrast, the wavy-trailing-edge bodies have principally two-dimensional shear layers until they separate from the wavy-trailing-edge, which makes these bodies less sensitive to wave steepness.

In § 4, we have seen that as the spanwise wavelength of the waviness introduced in the two-dimensional shear layers approaches $\lambda/D \approx 5.6$, vortex roll-up into a Kármán vortex street is suppressed for a minimum value of W/λ. We therefore make the conjecture that there is a critical spanwise perturbation which can be introduced into a pair of shear layers which alters their dynamics and discourages the roll-up into spanwise vortices for a minimum waviness amplitude. Physical scales which have a similar wavelength are the mode A wavelength ($\approx 5.5D$) of a straight, non-wavy square-section cylinder and the primary wavelength (spacing between same-sign vortices in a row of a Kármán vortex street). The waviness of the stagnation face can be thought of as forcing mode A at a subcritical Reynolds number.

6. Conclusion

A numerical investigation has been performed to understand the effects of introducing a leading-edge sinusoidal waviness to a square cylinder. The investigations were primarily performed at a Reynolds number of $Re = 100$ for which the non-wavy square cylinder has a purely two-dimensional Kármán type wake. The wavelength

λ and amplitude W of the waviness were varied, introducing different degrees of geometric three-dimensionality. From consideration of the wake topology and force characteristics, the effect of introducing a wavy stagnation face has been classified into five distinct regimes.

For a mild geometric waviness we obtain regime I, where the formation of the wake at the base of the cylinder is mildly three-dimensional and the force history is similar to the straight cylinder. However as the wake evolves further downstream there is a discernible deformation of the spanwise Kármán vortices.

For a slightly higher level of waviness we obtain a transitional regime denoted as regime II. In this regime the effects of the geometric waviness in the formation region are more dominant. A large spanwise curvature appears in the top and bottom shear layers and an associated drop occurs in mean drag and the root mean square of the lift. Further downstream we observe the formation of streamwise vortices associated with the sinusoidal spanwise deformation of the distorted Kármán vortices. Within this transitional regime II, we make a further distinction between normalized wavelengths above and below $\lambda/D \approx 5.6$. For $\lambda/D \leqslant 5.6$, denoted as regime II (type A), we observe a time-periodic state with a single frequency where streamwise vortices occur in the braids and connect adjacent Kármán vortices. These streamwise vortices have some analogy with the streamwise structures found in the wake of a wavy splitter plate (for example, Meiburg & Lasheras 1988) and the mode A instability (see Williamson 1996*a*). However for $\lambda/D > 5.6$, denoted as regime II (type B), we observe a beating phenomenon where the wake topology alternates between a mildly three-dimensional state similar to regime I and a highly three-dimensional state similar to regime II (type A). Two distinct frequencies are detected, which again is similar to the results of Bearman & Tombazis (1993) and Tombazis & Bearman (1997) for a wavy-trailing-edge body with cellular vortex shedding and the associated vortex dislocations.

Finally, when the amplitude of the waviness is sufficiently large, we obtain a near-base region which is completely steady, leading to a significant reduction in mean drag and the lift tending to zero. This region of maximal drag reduction is denoted regime III and within this regime, there is no evidence of a Kármán vortex wake. Once again we can identify two sub-regimes. In the first case, regime III (type A), the flow is completely steady and has only been observed for $\lambda/D \leqslant 5.6$. It is in regime III (type A) that the most significant drag reduction occurs. However, when $\lambda/D > 5.6$, hairpin vortices are shed periodically from the almost steady near-base region. In this regime, defined as regime III (type B), a small unsteadiness appears in the near wake due to the shedding of these hairpin vortices. We note that the wake topology of the hairpin vortices in regime III (type B) resembles that of a sphere at low Reynolds numbers. It was shown that the smallest wave steepness W/λ to force the flow into regime III (type A) occurs at around a value of $\lambda/D \approx 5.6$. This critical wavelength has a similar length scale to the mode A transition of the wake of a straight, non-wavy square-section cylinder and the primary spacing of same-sign vortices in a Kármán vortex street.

The three-dimensional geometry produces a leading-edge cross-flow which generates streamwise and vertical components of vorticity in the early stages of the shedding process. These additional components of vorticity appear in regions close to the inflection points of the wavy stagnation face where the spanwise vorticity is weakened. They then persist in the top and bottom shear layers which distort the shear layers so that their vertical displacement is largest behind the most downstream cross-section and is smallest behind the most upstream cross-section. It is hypothesized that a sufficiently large spanwise perturbation of the shear layers alters their dynamic

interaction by diverting spanwise vorticity into streamwise and vertical components of vorticity, leading to the suppression of the Kármán street and an associated drop in drag.

For the wavy-leading-edge body, the perturbations in the vorticity distribution are introduced at the wavy stagnation face and so have a longer period of time to evolve than if these perturbations were introduced at the trailing edge. The wavy-leading-edge bodies are therefore more sensitive to wave steepness than the wavy-trailing-edge bodies. It would also appear that the introduction of a waviness at a wavelength close to the mode A and the primary wavelengths of the straight square-section cylinder leads the suppression of the Kármán street at a minimal waviness amplitude.

A drag reduction of 16% at $Re = 100$ was obtained as compared to a drag reduction of at least 30% achieved in the experiments of Bearman & Owen (1998*a*, *b*) at $Re = 40\,000$. This large variation is principally due to the fact that for a straight, non-wavy cylinder, the shear layers separate from the leading edge at $Re = 40\,000$ whereas at $Re = 100$ the shear layers remain attached until they separate from the trailing edge. The leading-edge separation at higher Reynolds numbers leads to a higher drag for the straight, non-wavy cylinder. However, from on-going simulations at $Re = 500$, the asymptotic level of the drag coefficient of the wavy cylinder does not change significantly from that at $Re = 100$. Therefore, at $Re = 500$, we would expect a higher drag reduction due to the increase in the drag coefficient of the straight, non-wavy cylinder.

The authors would like to acknowledge several inspiring discussions and critical feed-back from J. C. Owen, Professor P. W. Bearman and Professor F. Hussain. We also wish to thank Dr D. Barkley and Dr D. J. Doorly for their questions and comments. The first author is supported by the Overseas Research Students Awards Scheme administered by the Committee of Vice-Chancellors and Principals of the Universities of the United Kingdom and the Edmund Davis Trust fund awarded by the University of London. Computational resources were provided by the Computer Services for Academic Research (CSAR) at the University of Manchester under the EPSRC grant number GR/M08424 and the Imperial College Parallel Computing Centre.

Appendix. Discretization of the Navier–Stokes equations

The Navier–Stokes equations (equation (3.4)) are solved using the hybrid code $\mathcal{N}\boldsymbol{\varepsilon\kappa}\mathcal{T}\boldsymbol{\alpha r}$ (Sherwin & Karniadakis 1995; Warburton 1998; Karniadakis & Sherwin 1999). A Fourier expansion is used in the spanwise direction, while two-dimensional spectral elements are used in each of the Fourier planes. Within each triangular element both the solution and the geometry are represented by a higher-order polynomial basis which is C^o continuous across the elemental boundaries. Convergence can be achieved either by increasing the number of elements (h-convergence) or by increasing the polynomial order within each element (P-convergence). A convergence study involving both h and P convergence is given in § A.1 for the two-dimensional mesh.

A non-dimensional time step of $\Delta t U_\infty / D = 0.005$ was used with second-order time integration for most of the simulations. However, for large values of the wave steepness W/λ, it was necessary to decrease the time step to 0.0025 and use first-order time integration. Convergence tests indicated that the simulations were well resolved in time.

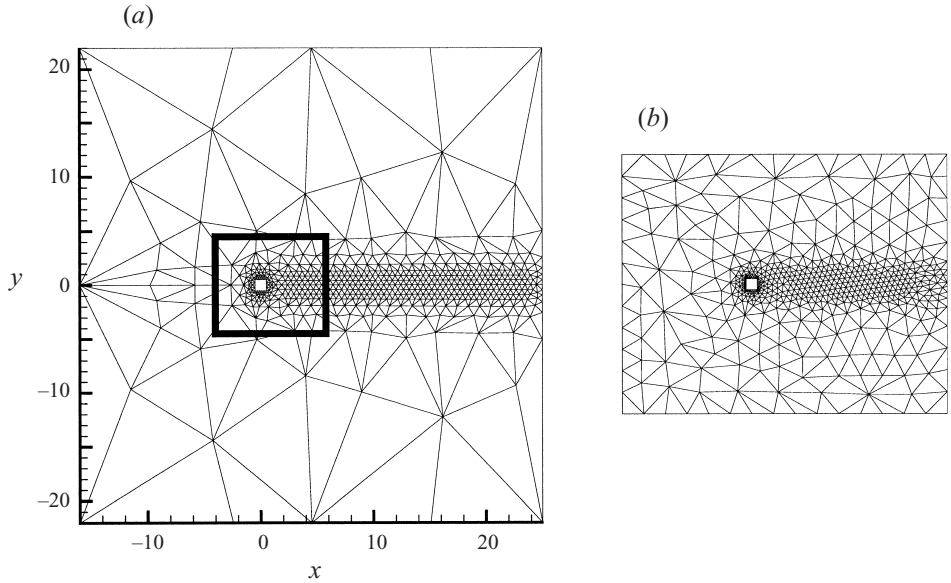

FIGURE 26. (*a*) Coarse spectral element mesh M1 (1110 triangles). The bold square indicates the region where an *h*-refinement was performed (see figure 27). (*b*) Smaller spectral element mesh M4 (1083 triangles). Note that mesh M4 is drawn to scale with respect to mesh M1.

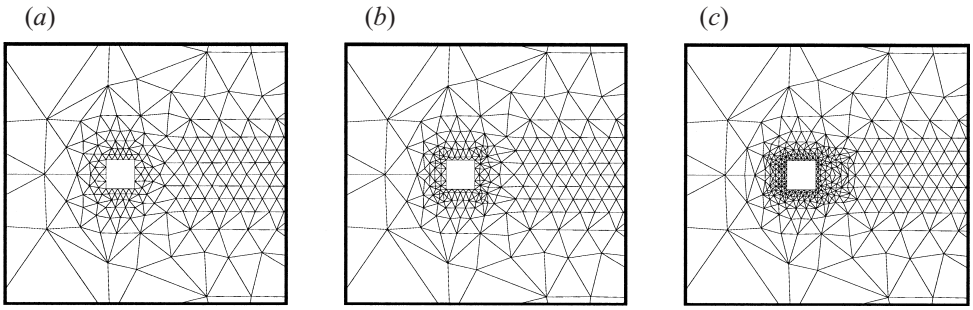

FIGURE 27. *h*-refinement near the wall. (*a*) M1; (*b*) M2; (*c*) M3.

A.1. *Convergence studies*

The detailed convergence study presented in Barkley & Henderson (1996) was used as the principal guide in the present study. They extensively tested the effects of the domain size parameters, l_i (inflow), l_o (outflow), l_h (crossflow) on the numerical solutions. Based on their chosen domain parameters which resulted in a mesh-independent solution, we have selected the following parameters for the present study: $l_i = 16$, $l_o = 25$, $l_h = 22$ (blockage $= \frac{1}{2}l_h \approx 2.3\%$). For the square-section cylinder, the resolution near the sharp corners and the walls is a critical point to consider as large gradients of the vorticity occur around these regions. It was therefore decided to investigate the effect of an *h*-refinement near the geometry while keeping the external resolution of the domain fixed. Three levels of mesh resolution were tested. The first level represents a coarse mesh denoted by M1 and has 1110 spectral elements (see figure 26*a*). The second level M2 corresponds to a medium mesh with a total of 1196 elements and finally the fine mesh M3 has 1502 elements. In each case, only the near-wall mesh has been refined whereas the rest of the domain is

Mesh/Polynomial order	St	C_D	C_{D_P}	C'_L	C'_{L_P}
M1, $P = 6$	0.1446	1.4626	1.3922	0.1822	0.1589
M2, $P = 6$	0.1447	1.4559	1.3896	0.1821	0.1590
M3, $P = 6$	0.1446	1.4613	1.3989	0.1845	0.1610
M1, $P = 8$	0.1446	1.4652	1.3956	0.1836	0.1601
M2, $P = 8$	0.1447	1.4627	1.3958	0.1836	0.1601
M3, $P = 8$	0.1446	1.4669	1.4052	0.1848	0.1613
M1, $P = 10$	0.1446	1.4652	1.3956	0.1848	0.1612
M2, $P = 10$	0.1446	1.4667	1.4007	0.1848	0.1612
M3, $P = 10$	0.1446	1.4664	1.4087	0.1852	0.1617
M4, $P = 6$	0.1463	1.4855	1.4324	0.1864	0.1628

TABLE 1. Convergence of global flow parameters at $Re = 100$ with polynomial order P for the various h-refinement levels.

kept at the same resolution (see figure 27). A smaller mesh with $l_i = 12$, $l_o = 18$, $l_h = 12$ (blockage $\approx 4.2\%$) shown in figure 26(b) was used to check the order of magnitude of the errors. Results are presented in table 1 for global flow coefficients St, C_D, C_{D_P}, C'_L, C'_{L_P} as the polynomial order, P, is increased for each of the various h-refinements at $Re = 100$. Here St is the Strouhal number ($St = fD/U_\infty$, where f is the vortex shedding frequency), C_D is the mean coefficient of total drag, C_{D_P} is the mean coefficient of the pressure drag, C'_L is the root mean square of the total lift coefficient and C'_{LP} is the root mean square of the pressure lift coefficient. For these tests, the time step was held constant at $\Delta t U_\infty/D = 0.005$ and second-order time integration was used.

All runs captured the large scales of motion in the wake, i.e. the vortex street. On the quantitative side, the variation between the values at $P = 6$ to $P = 10$ is less than 1%. The M3 mesh already provides accurate results at $P = 6$. In addition, the smaller mesh M4 provides a good basis to judge the level of errors. Even with these reduced dimensions and increase in blockage ratio, the maximum error is still less than 2% when compared to the high-resolution run (M3 with $P = 10$).

Based on this analysis, it was decided to use both meshes M3 and M4 at $P = 6$ with an error tolerance of 2%. Most of the runs with the M3 mesh have been performed at $P = 8$. Spot checks have also been done at higher resolution ($P = 9, 10$) during the convergence for some cases. Temporal convergence was also investigated by reducing the time step by half and did not show any difference in the global flow coefficients.

The spanlength of the computational domain, L_z, was chosen to be equal to one geometric wavelength, λ. Tests were performed with two wavelengths but did not show any difference in the forces and wake topology. The Fourier resolution in the spanwise direction was investigated for the particular case of $\lambda/D = 5.6$, $W/\lambda = 0.1667$. The number of Fourier modes required to reach the dissipation scale in the simulation can be estimated from $\beta_D = (2\pi/L_z)M \approx Re^{1/2}$ (Henderson 1997) or $M \approx 9$ modes for $\lambda/D = 5.6$ and $Re = 100$. Three different resolutions were tested with $8, 16, 32$ Fourier modes. In the saturated state, the values of the forces differed by only 0.3% and the wake topology was similar. Based on this analysis, it was decided to use eight Fourier modes for $\lambda/D \leqslant 4.0$ and 16 modes for $\lambda/D > 4.0$.

Simulation runs were performed on 8 and 16 DEC Alpha 21164 processors of a CRAY T3E-1200E, used 200 MB per processor and took about 7 seconds per time step.

REFERENCES

Barkley, D. & Henderson, R. D. 1996 Three-dimensional floquet stability analysis of the wake of a circular cylinder. *J. Fluid Mech.* **322**, 215–241.

Bearman, P. W. 1965 Investigation of the flow behind a two-dimensional model with a blunt trailing edge and fitted with splitter plates. *J. Fluid. Mech.* **21**, 241–255.

Bearman, P. W. 1967 The effect of base bleed on the flow behind a two-dimensional model with a blunt trailing edge. *Aero. Q.* **18**, 207–224.

Bearman, P. W. & Owen, J. C. 1998*a* Special Brief Note: Reduction of bluff-body drag and suppression of vortex shedding by the introduction of wavy separation lines. *J. Fluids Struct.* **12**, 123–130.

Bearman, P. W. & Owen, J. C. 1998*b* Suppressing vortex shedding from bluff bodies by the introduction of wavy separation lines. In *1998 ASME Fluids Engineering Division Summer Meeting*.

Bearman, P. W. & Tombazis, N. 1993 The effect of three-dimensional imposed disturbances on bluff body near wake flows. *J. Wind Engng Indust. Aero.* **49**, 339–350.

Evangelinos, C. 1999 Parallel spectral/hp methods and simulations of flow/structure interactions. PhD thesis, Brown University.

Henderson, R. D. 1997 Nonlinear dynamics and pattern formation in turbulent wake transition. *J. Fluid Mech.* **352**, 65–112.

Henderson, R. D. & Barkley, D. 1996 Secondary instability in the wake of a circular cylinder. *Phys. Fluids* **8**, 1683–1685.

Henderson, R. D. & Karniadakis, G. E. 1995 Unstructured spectral element methods for simulation of turbulent flows. *J. Comput. Phys.* **122**, 191–217.

Jeong, J. & Hussain, F. 1995 On the identification of a vortex. *J. Fluid Mech.* **285**, 69–94.

Johnson, T. A. & Patel, V. C. 1999 Flow past a sphere up to a Reynolds number of 300. *J. Fluid Mech.* **378**, 19–70.

Karniadakis, G. E. & Sherwin, S. J. 1999 *Spectral h/p Element Methods for CFD*, 1st Edn. Oxford University Press.

Karniadakis, G. E. & Triantafyllou, G. S. 1992 Three-dimensional dynamics and transition to turbulence in the wake of bluff objects. *J. Fluid Mech.* **238**, 1–30.

Lasheras, J. C. & Choi, H. 1988 Three-dimensional instability of a plane free shear layer: an experimental study of the formation and evolution of streamwise vortices. *J. Fluid Mech.* **189**, 53–86.

Lasheras, J. C. & Meiburg, E. 1990 Three-dimensional vorticity modes in the wake of a flat plate. *Phys. Fluids* A **2**, 371–380.

Meiburg, E. & Lasheras, J. C. 1988 Experimental and numerical investigation of the three-dimensional transition in plane wakes. *J. Fluid Mech.* **190**, 1–37.

Naumann, A., Morsbach, M. & Kramer, C. 1966 The conditions of separation and vortex formation past cylinders. In *AGARD Conf. Proc. No. 4, Separated Flows*, pp. 539–574.

Newman, D. 1996 A computational study of fluid/structure interactions: flow-induced vibrations of a flexible cable. PhD thesis, Princeton University.

Petrusma, M. S. & Gai, S. L. 1994 The effect of geometry on the base pressure recovery of the segmented blunt trailing edges. *Aeronaut. J.* **98**, 267–274.

Petrusma, M. S. & Gai, S. L. 1996 Bluff body wakes with free, fixed, and discontinuous separation at low Reynolds numbers and low aspect ratio. *Exps. Fluids* **20**, 189–198.

Robichaux, J., Balachandar, S. & Vanka, S. P. 1999 Three-dimensional floquet instability of the wake of square cylinder. *Phys. Fluids* **11**, 560–578.

Rodriguez, O. 1991 Base drag reduction by control of the three-dimensional unsteady vortical structures. *Exps. Fluids* **11**, 218–226.

Roshko, A. 1955 On the wake and drag of bluff bodies. *J. Aeronaut. Sci.* **22**, 124.

Sherwin, S. J. & Karniadakis, G. E. 1995 A triangular spectral element method: applications to the incompressible Navier–Stokes equations. *Comput. Meth. Appl. Mech. Engng* **123**, 189.

Sherwin, S. J. & Karniadakis, G. E. 1996 Tetrahedral *hp* finite elements: Algorithms and flow solutions. *J. Comput. Phys.* **124**, 14–45.

Sohankar, A., Norberg, C. & Davidson, L. 1998 Low-Reynolds number flow around a square

cylinder at incidence: study of blockage, onset of vortex shedding, and open boundary conditions. *Intl J. Numer. Meth. Fluids* **26**, 39–56.

TANNER, M. 1972 A method of reducing the base drag of wings with blunt trailing edge. *Aeronaut. Q.* **23**, 15–23.

THOMPSON, M., HOURIGAN, K. & SHERIDAN, J. 1996 Three-dimensional instabilities in the wake of a circular cylinder. *Expl Therm. Fluid Sci.* **12**, 190–196.

TOMBAZIS, N. & BEARMAN, P. W. 1997 A study of three-dimensional aspects of vortex shedding from a bluff body with a mild geometric disturbance. *J. Fluid Mech.* **330**, 85–112.

WARBURTON, T. 1998 Spectral/hp element methods on polymorphic multi-domains: Algorithms and applications. PhD thesis, Division of Applied Mathematics, Brown University.

WILLIAMSON, C. H. K. 1996*a* Three-dimensional wake transition. *J. Fluid Mech.* **328**, 345–407.

WILLIAMSON, C. H. K. 1996*b* Vortex dynamics in the cylinder wake. *Ann. Rev. Fluid Mech.* **28**, 477–539.

ZHANG, H.-Q., FEY, U., NOACK, B. R., KÖNIG, M. & ECKELMANN, H. 1995 On the transition of the cylinder wake. *Phys. Fluids* **7**, 779–794.